Available online at www.sciencedirect.com

ScienceDirect

ijmulflow

International Journal of Multiphase Flow 00 (2013) 1–51

Numerical study of single bubble motion in liquid metal exposed to a longitudinal magnetic field

S. Schwarz[1], J. Fröhlich

Institute of Fluid Mechanics, TU Dresden, 01062 Dresden, Germany

Abstract

The paper presents numerical simulations modeling the ascent of an argon bubble in liquid metal with and without an external magnetic field. The governing equations for the fluid and the electric potential are discretized in a uniform Cartesian grid and the bubble is represented with a highly efficient immersed boundary method. The simulations performed were conducted matching experiments under the same conditions so that sound validation is possible. The three-dimensional trajectory of the bubble is analyzed quantitatively and related to the flow structures in the wake. Indeed, the substantial impact of the magnetic field in the bubble trajectory results from its influence on the wake. Quantitative data describing the selective damping of vortex structures are provided and discussed. As a result of applying a longitudinal field, the time-averaged bubble rise velocity increases for large bubbles, it reaches a local maximum and then decreases when increasing the magnetic interaction parameter. For small bubbles, the time-averaged bubble rise velocity decreases when increasing the magnetic field. The bubble Strouhal number as a dimensionless frequency is reduced with the application of a magnetic field for all bubbles considered and the zig-zag trajectory of the bubble becomes more rectilinear. All this is traced back to the modification of vortical structures in the bubble wake due to the magnetic field.

Keywords: immersed boundary method, bubble, magnetohydrodynamics, liquid metal

1. Introduction

The ascent of a single bubble in a quiescent liquid is a fascinating phenomenon, for the layman as well as for the scientist. The trajectory of the bubble which can exhibit forms ranging from straight vertical ascent to chaotic irregular motion, and regimes of shape ranging from strictly spherical to

Email addresses: Stephan.Schwarz@tu-dresden.de (S. Schwarz), Jochen.Fröhlich@tu-dresden.de (J. Fröhlich)

[1]Corresponding author

irregularly wobbling still challenge physicists and engineers. An interesting review assembling the early knowledge on rising bubbles is given in [1]. In this reference, the term Leonardo's paradoxon is suggested for the tendency of sufficiently large bubbles to rise along a zig-zag or spiraling path rather than along a rectilinear one. The reason for the latter is attributed to the structure of the bubble wake. Two-threaded vortices of opposite circulation induce a lift force on the bubble deflecting it from a strictly vertical trajectory. A review on the hydrodynamic forces acting on isolated, spheroidal high-Reynolds-number bubbles and the associated motion is provided in [2]. The vortical structures in the wake of air bubbles in water have been analyzed by modern optical experimental techniques like Schlieren optics [3], digital particle image velocimetry [4] or dye visualization [5]. Alternately shed vortex filaments are observed for a bubble rising in zig-zag, while a spiral trajectory is characterized by a continuous pair of parallel vortices wrapped around the axis of the helix. In experiments, it has been observed frequently that the path first follows a zig-zag and later on changes to a helical shape [6, 7], whereas a transition in the opposite direction has not been reported so far. Not surprisingly, the structures in the wake behind bubbles rising in zig-zag are similar to those observed behind rising solid spheres following a zig-zag trajectory [8]. It has been shown experimentally [9] as well as numerically [10, 11, 12] that path oscillations can appear in the absence of shape oscillations which proves that indeed the vortex structures in the wake are responsible for the former. This is extensively discussed in the review of Ern et al. [13] which assembles current knowledge about the wake of fixed bodies and its relation to the onset and development of path instabilities of both bubbles and rigid objects.

Most experimental and numerical work on bubbles so far has been conducted for the air-water system, often using hyper-clean water which is almost free of contaminants and therefore justifies the application of a shear-free boundary condition at the gas-liquid interface [2, 12]. Nevertheless, there is a variety of industrial applications where gas bubbles play an important role and where these conditions are not met. The continuous casting process in metallurgy is one example [14, 15]. Here, gas bubbles are injected into the melt to clean the liquid metal from contaminants and to stir and homogenize the liquid phase [16]. Magnetic fields are used in liquid metal processes to stir [17] and to stabilize the flow regimes [18]. Liquid metals are prone to oxidation, and in general a melt is never free of contaminants so that an oxide layer forms at the gas-liquid interface. Furthermore, contaminants and inclusions agglomerate at the bubble surface. The appropriate condition for the velocity at the bubble surface hence is the no-slip condition. This is backed by the observation that

the drag of a fully contaminated spherical bubble corresponds to that of a solid sphere [2, 19].
To illustrate the parameter range considered in the present work, Table 5 lists material properties of the eutectic alloy GaInSn and compares them to those of water. The definition of the non-dimensional numbers is given in Section 2.1 below. The alloy GaInSn is representative of a general liquid metal and has been selected here because the simulations reported below have been conducted for a configuration with argon bubbles in GaInSn which is liquid at room temperature, an attractive property for its use in experiments. Its density and surface tension are markedly higher than those of water, while the kinematic viscosity is smaller. As a consequence, the Galilei number which relates buoyancy forces to viscous forces is higher for an argon bubble in GaInSn than for an air bubble of equal size in water, hence resulting in a higher bubble Reynolds number. The high density ratio and high surface tension are difficult to deal with in many multiphase methods, e.g. the volume of fluid method where spurious currents may occur as numerical artifacts and small time step sizes become necessary. The most significant contrast with water is the difference in electrical conductivity by about eight orders of magnitude. An approximate value for tab water is listed for comparison. The Eötvös number relating buoyancy force to surface tension forces is almost the same, so that in GaInSn similar bubble shapes as in water can be expected for a given diameter. According to the review of Loth [20], or extrapolating the regime map of Clift et al. [21], the shape of an argon bubble with diameter around 5 mm in GaInSn is expected to be 'ellipsoidally wobbling', in the sense that it is close to ellipsoidal with the axes of the ellipsoid varying in time.

Liquid metals are opaque and therefore experimental data are difficult to obtain and rare. The optical measurement techniques specified above hence cannot be used to get detailed insight into liquid metal multiphase flows. Ultrasound Doppler velocimetry is an alternative approach in this case and has been used to study the motion of a single bubble [22] and a bubble-driven liquid metal jet [16] under the influence of magnetic fields. Local conductivity probes have also been used to measure the rise velocity of bubbles in mercury [23] as well as the behavior of gas bubbles in turbulent liquid metal magnetohydrodynamic flows [24, 25].
Direct numerical simulation of bubbles in liquid metals is challenging due to the large differences of density and viscosity between the phases and the high bubble Reynolds number typically encountered. As a result, there are only very few phase-resolving simulations of bubbles in liquid metal under the influence of a magnetic field. A rising bubble in a small enclosure under a vertical magnetic field was computed in [26] by means of a Volume of Fluid approach with reduced density and

viscosity ratio and very moderate Galilei number. Gaudlitz and Adams [27] simulated the influence of a vertical magnetic field on the rise of a single bubble in electrically conductive liquids with a hybrid particle level set method neglecting the effect of interface contamination. The numerical parameters of this case correspond to a small bubble in mercury, i.e. the Galilei number is smaller by a factor of five compared to the present study.

It is known that homogeneous magnetic fields substantially modify vortical structures in turbulent flows [28, 29] as well as the pressure field around fixed objects [30]. Therefore, a considerable impact of such a field on the bubble dynamics is to be expected [31],which indeed was observed in experiments [22, 16]. Despite these studies the actual influence of a magnetic field on bubbles in liquid metal is still not fully understood. In particular, the impact of a magnetic field on the interaction between bubble wake and bubble dynamics in metallurgical systems is unclear and also the modification of the bubble shape in that case is not fully understood to this date. This is mostly due to the lack of visual data impeded by the opaque liquid metal.

The aim of the present paper is to fill this gap and to provide insight into the influence of a longitudinal magnetic field on bubble wake and bubble dynamics. Phase-resolving direct numerical simulations of an argon bubble in the liquid metal GaInSn have been conducted for different values of magnetic interaction. The three-dimensional data of high spatial and temporal resolution obtained from the simulations are evaluated, visualized and compared against experimental data.

The paper is structured as follows: Section 2 gives a short description of the equations to be solved and the numerical approach employed, as well as a refinement study quantifying the numerical error. Section 3 contains the numerical results for the ascent of a single bubble with and without a magnetic field. Visualizations are presented to highlight conspicuous flow features in the bubble wake. Furthermore, the numerical results are compared against available experimental findings and other simulation data. The last section summarizes the results of the present study and outlines future research directions.

2. Method

2.1. Parameters of single bubble ascent

The problem of a single particle rising or falling in a pool of quiescent fluid due to the effect of buoyancy is governed by three parameters [13]: The particle-to-fluid density ratio $\pi_\rho = \rho_p/\rho_f$, the Galileo number $G = \sqrt{|\pi_\rho - 1|\, g\, d_{eq}^3}/\nu$, and a geometrical parameter relating to the shape of the particle, such as the ratio of diameter to height for a cylindrical particle or the aspect ratio for an ellipsoid of rotation, for example. Here, g is gravity, d_{eq} is the diameter of a volume-equivalent sphere and ν is the kinematic viscosity of the liquid. In the following we will use the terms bubble and particle practically as synonyms, with index p throughout. Indeed, the term 'particle' in the literature often designates any element of a disperse phase, be it solid, fluid or gaseous [21]. In case of a rising bubble, the density ratio is very small and the motion is predominantly governed by the inertia of the fluid. The Galileo number, which is the square root of the Archimedes number, determines the ratio of the driving buoyancy force to the viscous forces. Inserting the gravitational velocity $u_{ref} = \sqrt{|\pi_\rho - 1|\, g\, d_{eq}}$ into the definition of G yields a reference Reynolds number Re_{ref}. The latter velocity scale, u_{ref}, and in a similar fashion the reference time $t_{ref} = \sqrt{d_{eq}/(|\pi_\rho - 1|\, g)}$ are used for scaling here, together with the reference length d_{eq}.

The shape of a single rising bubble is governed by viscous and pressure forces deforming the interface and by the stabilizing effect of surface tension driving the bubble shape towards a spherical one. The Eötvös number $Eo = \Delta\rho\, g\, d_{eq}^2/\sigma$ which is the ratio of buoyancy force to surface tension force therefore can be used to characterize the bubble shape. Here, $\Delta\rho$ denotes the density difference between the phases and σ the surface tension. The three parameters G, π_ρ and Eo characterize the system and are known *a priori*.

The bubble velocity $\mathbf{u}_p = (u_p,\, v_p,\, w_p)^T$ is a result of the simulation. The rise velocity v_p can then be used to determine the bubble Reynolds number $Re = v_p\, d_{eq}/\nu$. The instantaneous, vertical component of the bubble velocity is used here to calculate $Re(t)$ because this component was measured in the corresponding experiments [22]. The Weber number is defined as $We = \rho_f\, |\mathbf{u}_p|^2\, d_{eq}/\sigma$ using the absolute value of the bubble velocity. The instantaneous Weber number $We(t)$ is used to characterize the time-dependent bubble shape as discussed in Section 2.3 below.

Finally, a non-dimensional number needs to be introduced to quantify the relative strength of magnetic forces. This can be done by the magnetic interaction parameter $N = \sigma_e\, B^2\, d_{eq}/\,(\rho_f\, u_{ref})$, also termed Stuart number, representing the ratio of magnetic forces to inertial forces [22, 28].

2.2. Continuous phase

In the present work, an Euler-Lagrange approach is chosen for the phase-resolving simulation of the ascent of a single bubble in liquid metal. The simulations presented here were carried out with the in-house multiphase code PRIME [32]. The equations for the continuous phase are solved on a Cartesian grid with staggered grid arrangement employing a second-order finite volume method. A Runge-Kutta three-step method with implicit treatment of the viscous terms by a Crank-Nicolson scheme is used for time integration. Further details of the code, the discretization of the equations and their numerical treatment are provided in the cited reference.

The incompressible Navier-Stokes equations including the Lorentz force read

$$\nabla \cdot \mathbf{u} = 0\,, \tag{1}$$

$$\frac{\partial \mathbf{u}}{\partial t} + (\mathbf{u} \cdot \nabla)\,\mathbf{u} = -\frac{1}{\rho_f}\nabla p + \frac{1}{Re_{ref}}\nabla^2 \mathbf{u} + N\,(\mathbf{j} \times \mathbf{B}) + \mathbf{f}\,, \tag{2}$$

with the usual nomenclature $\mathbf{u} = (u,\, v,\, w)^T$ being the velocity of the continuous phase along the Cartesian coordinates x, y, z. Furthermore, p is the pressure, $\mathbf{j}$ the electric current density, $\mathbf{B}$ the magnetic field and $\mathbf{f}$ a specific volume force.

For small values of the magnetic Reynolds number, the magnetic field induced by the fluid motion is negligible compared to the applied magnetic field [28]. This situation is encountered in the present case. The magnetic Reynolds number, $R_m = \mu_0 \sigma_e d_{eq}\, u_{ref} \approx 4 \cdot 10^{-3}$, is indeed substantially smaller than unity and the quasi-static approximation is justified. Here, the physical properties of Table 5 for an Argon bubble in GaInSn were employed and μ_0 is the magnetic permeability of free space. Ohm's law then allows to express the current density $\mathbf{j}$ by

$$\mathbf{j} = \sigma_e\,(-\nabla\Phi + \mathbf{u} \times \mathbf{B})\ , \tag{3}$$

with Φ denoting the electric potential [33].

The electric conductivity for both phases is modeled to be the same in most of the present study. This is adequate here as the focus is on the influence of a magnetic field on the bubble wake. The assumption is scrutinized in Section 3.6.2. Under the present conditions, charge conservation $\nabla \cdot \mathbf{j} = 0$ yields a Poisson equation for the electric potential Φ

$$\nabla^2 \Phi = \nabla \cdot (\mathbf{u} \times \mathbf{B}) \tag{4}$$

which is solved in a similar fashion as the pressure correction employed to satisfy equations (1) and (2).

2.3. Disperse phase

With the present approach, the bubbles are numerically represented by an immersed boundary method (IBM) [34] with extension to non-spherical particles and low particle densities proposed in [35, 32]. The surface of each individual bubble is described using a set of Lagrangian marker points interconnected by a triangular mesh (Figure 1a). The coupling between the embedded bubble and the liquid metal is realized by introducing additional volume forces $\mathbf{f}$ in the right hand side of (2) which are localized at the bubble surface and which impose a no-slip condition between the phases [34] as discussed in the introduction. In a recent study of the present authors [36], an extensive discussion is provided on the type of boundary condition to be applied and the respective justification in terms of physical and numerical modeling.

The motion of a single bubble is obtained by solving its linear and angular momentum equation

$$m_p \frac{d\mathbf{u}_p}{dt} = \rho_f \oint_S \boldsymbol{\tau} \cdot \mathbf{n}_S \, ds + V_p(\rho_p - \rho_f)\, \mathbf{g} \,, \tag{5}$$

$$\frac{d\,(\mathbf{I}_p \boldsymbol{\omega}_p)}{dt} = \rho_f \oint_S \mathbf{r} \times (\boldsymbol{\tau} \cdot \mathbf{n}_S)\, ds \,. \tag{6}$$

Here, $\mathbf{u}_p$ and $\boldsymbol{\omega}_p$ designate the linear and angular velocity of the particle, while m_p denotes its mass, and $\mathbf{I}_p$ its tensor of inertia. Furthermore, $\boldsymbol{\tau}$ is the hydrodynamic stress tensor divided by the fluid density, including contributions from pressure and viscous stresses, while $\mathbf{n}_S$ denotes the outward-pointing normal vector of the interface S, i.e. the bubble surface. The vector $\mathbf{r}$ identifies a point on S with respect to the position of the center of mass of the particle $\mathbf{x}_p$. The buoyancy force appears on the right hand side of (5) as a source term proportional to the density difference since the hydrostatic component in the continuous pressure field p has been eliminated in (2). The equations of motion (5) and (6) are solved and $\mathbf{u}_p$ and $\boldsymbol{\omega}_p$ are integrated in time to determine the bubble position $\mathbf{x}_p$ and inclination $\boldsymbol{\phi}$ as a function of time. The inclination angles are defined according to standard rotation matrices in xyz-convention of a Cartesian coordinate system centered in $\mathbf{x}_p$ [37]. For details on the numerical solution of equation (5) and (6) as well as on the phase coupling, we refer to [32, 34, 38, 39].

In the present study, the bubble shape is approximated as an oblate ellipsoid of rotation with aspect ratio $X = a/b$ and semi-axes $a = c > b$ (Figure 1b). For the parameters of an argon bubble in GaInSn, the bubble shape is expected to be 'ellipsoidally wobbling' [21]. Hence, the shape parameter X of the ellipsoidal particle has to be varied in time in a physically meaningful way. As suggested in [20], an empirical correlation between the instantaneous bubble Weber number $We(t)$ and the instantaneous aspect ratio $X(t)$ is employed here. Loth [20] presented experimental and theoretical data for the correlation $X(We)$ and provided a fit for moderate to high bubble Reynolds numbers $Re > 100$. The correlation was obtained using data for the mean rise velocity and mean aspect ratio. It is then shown in [20] that the correlation is also a good fit for instantaneous data $X(We(t))$ by comparing to the experiments of [7]. For the present parameter range with $Re > 100$, the correlation reads

$$X^{-1}(t) = 1 - 0.75 \tanh(0.165\, We(t)) \, , \tag{7}$$

with $We = \rho_f \, |\mathbf{u}_p|^2 \, d_{eq}/\sigma$. Figure 7 shows this curve together with the data given in the review of Loth [20]. With the material properties being constant, a bubble moving with a high velocity $|\mathbf{u}_p(t)|$ will adopt a flat shape while the bubble shape remains spherical at low velocities. Note that for very large Weber numbers the bubble in reality adopts a cap-like shape instead of an ellipsoidal shape. In the parameter range studied here, however, the assumption of an ellipsoidal bubble shape is very well justified [21].

It is a useful feature of the employed method that the particle shape can be modeled directly. The shape of each individual particle is analytically prescribed and therefore the constraint of constant volume can easily be implemented. In this way the bubble mass can be conserved exactly. Furthermore, experimental information on the bubble shape, if available, can be introduced. The delicate evaluation of surface curvature and the introduction of surface tension forces are not needed in the present model. This yields high robustness and avoids spurious currents [40]. An exactly defined phase boundary, in contrast to a diffuse interface, is also advantageous for the modeling of particle-particle and particle-wall interactions [41].

Since liquid metals are practically always contaminated by oxides a no-slip condition at the bubble surface is physically the most reasonable one as discussed above. Therefore the fluid velocity at the bubble surface S is imposed to equal the local surface velocity of the bubble at each Lagrangian forcing point. The latter velocity consists of three parts,

$$\mathbf{u}_S(\mathbf{r},\, t) = \mathbf{u}_p + \boldsymbol{\omega}_p \times \mathbf{r} + \mathbf{u}_{sh} \ , \tag{8}$$

where $\mathbf{u}_p$ is the translational velocity of the particle center resulting from equation (5), while the second term denotes the part due to rotation calculated from equation (6). Finally, $\mathbf{u}_{sh}$ is the velocity induced by changes in the shape resulting from an instantaneous change in the ellipsoid aspect ratio $X(t)$ as illustrated in Figure 1. The Lagrangian surface mesh is adapted to the instantaneous shape $X(t)$ in each time step by rescaling its relative coordinates with respect to the bubble center according to the change in aspect ratio.

2.4. Refinement study

A grid refinement study was carried out to estimate the numerical error of the spatial and temporal discretization and to determine the overall order of convergence of the method in the present setup. It was conducted for the initial phase of the ascent during which the bubble accelerates and changes its shape from spherical to ellipsoidal with $X \approx 1.5$. Refinement is performed simultaneously for the spacing of the equidistant Cartesian grid, the Lagrangian surface mesh and the time step. Consequently, the CFL number remains approximately constant. The number of forcing points n_L on the surface of an oblate ellipsoid is related to the mesh size Δx of the equidistant Cartesian grid by

$$n_L \gtrsim \frac{\pi}{3}\left(\frac{d_{eq}^2\left(2X^{-1/3}+X^{2/3}\right)}{\Delta x^2}+1\right) \tag{9}$$

for an even distribution of Lagrangian surface markers. The relation is obtained following the procedure derived for a sphere in [34] under the constraint $\Delta V_L \approx \Delta x^3$, where ΔV_L is the partial volume associated with a single Lagrangian forcing point. In the present implementation, it is possible to use more than the minimum required number of forcing points, i.e. a denser distribution of marker points on the surface by adjusting the volume ΔV_L according to the local density of marker points on the surface.

The refinement study was conducted in a cubic domain of extent $L = 6.0\,d_{eq}$ in all three directions, and an equidistant grid of n^3 points was used with periodic boundary conditions in all three directions. Gravity acts in negative y-direction. The setup basically corresponds to the one of the simulations presented later on, where a significantly longer extent of the computational domain in vertical direction was used, though. A single bubble is considered with a Galilei number of $G = 2825$, an Eötvös number of $Eo = 2.5$ and a density ratio of $\pi_\rho = 10^{-3}$ corresponding to a 4.6 mm argon bubble in GaInSn. Note that with $\pi_\rho \ll 1$ the results become independent of ρ_p. The particle is initially at rest, $\mathbf{u}_p = 0$, $\boldsymbol{\omega}_p = 0$, in quiescent fluid i.e. $\mathbf{u} = 0$ in the whole domain. The initial bubble position was chosen to be $\mathbf{x}_{p,0} = (3.0,\, 0.54,\, 3.0)\,d_{eq}$. According to the shape correlation (7) the bubble has a spherical shape, $X_0 = 1.0$, at the beginning of the simulation. A small initial inclination angle of $\boldsymbol{\phi}_0 = (0,\, 0,\, 0.05)\,\pi$ was applied which is of no relevance for a sphere, but gives a very small bias towards a zig-zag in the $x-y$-plane once the bubble starts to deform.

We consider the initial acceleration of the bubble for a fixed duration $t_{sim} = 3$ in dimensionless time units, roughly sufficient for the bubble to reach its terminal velocity. The temporal evolution of the bubble Reynolds number (based on v_p) is shown in Figure 3 for different numerical resolutions. At the end of the simulation, $t = t_{sim}$, the bubble has traveled a distance in y of about $3\,d_{eq}$, corresponding to slightly more than half the size of the computational domain (Figure 4.)

The discretization error is estimated at $t_e = 1.0$ by comparison of the computed instantaneous particle Reynolds number with the value obtained using the finest grid. In the reference case, the Eulerian grid has a spatial resolution of $n = 512$ corresponding to $d_{eq}/\Delta x = 85.3$ gridpoints over the equivalent diameter and a total number $134.2 \cdot 10^6$ cells. A set of $n_L = 24976$ Lagrangian forcing points was used in this case to represent the bubble surface and a non-dimensional time step of $\Delta t = 1.25 \cdot 10^{-3}$ was employed. By means of the fit depicted in Figure 5, excluding the two coarsest grids, a convergence order of about 1.7 is obtained for the systematically refined grids employed. The fluid discretization alone is second order accurate for single-phase simulations [42]. The direct forcing scheme utilized with the immersed-boundary method for coupling the dispersed phase to the fluid yields a reduction of the order of convergence [43]. The result for the present configuration is in line with the data in [32].

Based on the results of the refinement study, the resolution $n = 256$ was chosen for the simulations in the large computational domain. With an error of about 4%, it provides a good compromise between accuracy and computational effort. Further refinement would exceed the available computational resources. The chosen resolution therefore does not correspond to a full DNS, but will be adequate to provide valuable and detailed insight into the physics of this magnetohydrodynamic multiphase flow. Interpreting the results of the refinement study in physical terms we find that the time scale for the initial acceleration of the bubble is longer on coarser grids. A coarse resolution also yields higher Reynolds numbers at the end of these simulations (see Figure 3).

3. Results

3.1. Simulation of a single bubble without magnetic field

3.1.1. Setup of simulation without magnetic field

This section presents a simulation of a single bubble in liquid metal without magnetic field and a comparison against the experimental data of [22]. The physical parameters of the bubble correspond to those used for the refinement study above, $G = 2825$, $Eo = 2.5$ and $\pi_\rho = 10^{-3}$, which relate to an argon bubble with $d_{eq} = 4.6$ mm in eutectic GaInSn. As no magnetic field is applied, the magnetic interaction parameter is $N = 0$.
Compared to the refinement study, the computational domain was enlarged in the direction of gravity to resolve as much as possible of the bubble dynamics. The box extends over $\mathbf{L} = (L_x,\, L_y,\, L_z) = (6.0,\, 30.0,\, 6.0)\, d_{eq}$ and was discretized with a spatial resolution of $\mathbf{n} = (256,\, 1280,\, 256)$ points yielding a total of 83.9 Mio cells of the Eulerian grid. The bubble was represented with $n_L = 9093$ Lagrangian forcing points distributed over its surface. The time step is $\Delta t = 2.5 \cdot 10^{-3}$ in dimensionless units. Boundary conditions and initial conditions are the same as in the refinement study of Section 2.4, i.e. periodic conditions were applied in all three directions while the fluid as well as the bubble were initially at rest.

3.1.2. Setup of experiment and justification of box size

In the experiments by Zhang et al. [22], an open cylindrical container with a diameter of $D = 100$ mm and a height of $H = 220$ mm was used corresponding to $D \times H \approx (22 \times 48) d_{eq}$ for $d_{eq} = 4.6$ mm. The bubble was injected at the bottom center. A box with a quadratic cross section $(L_x \times L_z)$ is used in the present study for technical reasons with periodic boundary conditions which mimic a somewhat larger domain. Due to the high computational cost, especially the horizontal extension had to be reduced whereas a moderate reduction was chosen concerning the height. The areal blockage $\pi d_{eq}^2 / (4 L_x\, L_z)$ is about 2%. Gaudlitz [44] used a lateral extent of only $4 d_{eq}$, also with periodic boundary conditions, for a simulation of single bubble ascent at lower Re. It has been shown in [45] that the added mass coefficient of a spherical bubble horizontally aligned with a second bubble equals the one of a single bubble if the distance exceeds $3 d_{eq}$. The wake of two spheres placed side by side in uniform flow is only very weakly coupled if the spacing is larger than $3.5 d_{eq}$ [46]. A sphere next to a solid wall was studied in [47]. In [48] it is shown that for the largest Reynolds number considered, $Re = 300$, and a wall distance of $4d_{eq}$, drag and lift as well as the Strouhal number deviate only slightly from the values obtained in an unbounded fluid. For these reasons the horizontal extent of the computational domain selected for the present study in combination with periodic boundary conditions is adequate to represent the conditions of the experiments in the wide cylinder.

3.1.3. Results of the simulation and comparison with experimental data

A runtime of 60×61.5 CPU hours on 60 cores of an SGI Altix 4700 is needed for one crossing of the above box taking about 30 dimensionless units in time. The bubble Reynolds number based on the vertical velocity v_p is plotted over time in Figure 7. After an initial acceleration the bubble rise velocity starts to oscillate quasi-periodically. The corresponding experimental data of [22] are displayed in the same graph for comparison. These data were obtained using single-sensor ultrasound Doppler velocimetry which allows to measure the velocity component along a line.
An overview of the characteristic figures calculated from the instantaneous Reynolds number $Re(t)$ is given in Table 2, where $Re_t = \langle Re \rangle_t$ denotes the average rise Reynolds number obtained from a time average over the interval $t \in (6, 29.2)$, in the present case, and σ_{Re} the corresponding standard deviation. The average rise Reynolds number is in excellent agreement with the data from the measurements. Concerning the oscillation in $Re(t)$, an underestimation of the amplitude characterized by σ_{Re} is recognized. Asymmetric bubble deformation, i.e. a deviation from an ellipsoidal shape, and partial slip at the bubble surface in the experiment might be the reasons for the deviation, besides the remaining discretization error discussed in Section 2.4. The frequency on the other hand agrees well with the value reported in [22]. The dominant frequency f_{Re} of the oscillation in $Re(t)$ was obtained from the Fourier spectrum by means of a discrete Fourier transform (DFT) of Re computed with a Hanning window function to account for the non-periodic time signal. In addition, the frequency was determined from the roots in $Re(t) - Re_t$ and in the original experimental work of [22] by a least square curve fit to a sine function. Comparing the results to some extent assesses the uncertainty in the determination of f_{Re} due to the irregular oscillation and the limited period of time.

3.1.4. Additional data, interpretation and comparison with literature

Only the vertical component of the bubble velocity over time could be determined in the experiments [22] due to the measurement technique employed. The present simulations now offer full access to all velocity and pressure data for the continuous liquid metal phase as well as 3D data of the bubble trajectory. Therefore the simulations can deliver valuable complementary information on the bubble dynamics. This is reported in Figure 8 and Figure 9. Indeed, a zig-zag trajectory with lateral drift is observed in Figure 8 as conjectured by the experimentalists [22]. The maximum in $Re(t)$ occurs at extreme points of the bubble path $x_p(t)$. In these points, the bubble is oriented with its small semi-axis parallel to the gravity vector, i.e. the inclination angle ϕ_z is approximately zero. The amplitude of the zig-zag, measured between two extreme points of the path, is approximately $\Delta_{xz} = 1.15\, d_{eq}$. An oscillation in bubble inclination is found as well and plotted in Figure 9. The temporal change in the orientation $\phi_3 = \phi_z$ is clearly associated with the zig-zag along x. Maximum tilting of the bubble is found closely after a local minimum in $Re(t)$ and approximately half way between the turning points of the zig-zag trajectory where the lateral velocity is largest. Towards the end of the simulation and with the onset of the lateral drift the other two rotation angles ϕ_1, ϕ_2 also deviate from zero and oscillate with a higher frequency. The maximum inclination angle is found to be $|\phi_z|_{max} \approx 36°$.

These values can be compared to data from the literature. Lateral distances between two extreme points in a zig-zag trajectory of $1.0 \ldots 1.3\, d_{eq}$ and a maximum tilting of $27 \ldots 30°$ are reported for air-water experiments [49, 4] and for simulations of air bubbles in water [44, 11] at lower Reynolds numbers.

Due to high contamination and oxidation of the gas-liquid metal system a no-slip boundary condition is used here on the bubble surface as justified above. Therefore, besides the higher Reynolds number of the present simulation also the boundary condition at the bubble surface differs from the aforementioned simulations for air bubbles in water. Markedly larger inclination angles are reported for rigid spheroids compared to bubbles in clean water [2], and it is found in [13] that oblate bodies may follow highly non-linear trajectories with large rotation rates if the Reynolds number is high enough. After the initial transient in the present simulations the aspect ratio of the oblate ellipsoid determined according to equation (7) oscillates in the interval $X \in [1.35;\ 1.57]$. The bubble shapes for the mean, the minimum and the maximum aspect ratio are displayed in Figure 1 to convey an impression of the amount of shape modification during the presented simulation.

3.1.5. Simulation of a smaller bubble

A smaller bubble with $G = 1488$, $Eo = 1.05$ corresponding to an argon bubble of $d_{eq} = 3.0$ mm in GaInSn was studied as well. The parameters were adjusted in the simulation by changing viscosity and surface tension with all other parameters unchanged. For this smaller bubble, the time-averaged Reynolds number is $Re_t = 1822$. The change in surface tension yields different instantaneous Weber numbers and therefore different instantaneous aspect ratios from the correlation (7). The shape of this bubble remains almost spherical in this regime. The rise velocity again oscillates around its mean and a zig-zag path is observed. The characteristic frequency, calculated from a Fourier spectrum of $Re(t)$, is $f = 0.222$ which is in good agreement with the data of [50] for an air bubble in water at similar Re_t. In [50], the non-dimensional frequency is determined from vortex shedding visualized by optical measurements. If Re is high enough, a lock-in occurs between vortex shedding and oscillations in the rise velocity of bubbles. No experiments in liquid metal were conducted for this small bubble.

3.2. Simulation of a single bubble with magnetic field

3.2.1. Setup of simulation with magnetic field

A longitudinal, homogeneous magnetic field in the direction of gravity is now applied with the magnetic interaction parameter being $N = 0.5$ and $N = 1.0$, respectively. All other parameters are the same as for the simulation with $N = 0$ reported in the previous section. Only the domain size was increased in y-direction to $\mathbf{L} = (6.0,\ 48.0,\ 6.0)\, d_{eq}$ with a mesh of $\mathbf{n} = (256,\ 2048,\ 256)$, i.e. 134.2 Mio grid points. A longer box size in the direction of ascent is necessary because the zig-zag becomes stretched out and the characteristic frequency decreases under the impact of a magnetic field as will be shown later. This box size now corresponds to the height of the experimental container of 220 mm for the $d_{eq} = 4.6$ mm bubble.

3.2.2. Overview of results

A longitudinal magnetic field has significant impact on the bubble dynamics. The influence of the magnetic field is now discussed for a single ascending bubble with the parameters $G = 2825$ and $Eo = 2.5$. Quantitative results of the simulations are summarized in Table 3. When applying a longitudinal magnetic field this bubble rises faster and the oscillations in $Re(t)$ are damped as shown in Figure 10. The maximum inclination of the bubble decreases from $|\phi_z|_{max}(N = 0) \approx 36°$ in the absence of a magnetic field to $|\phi_z|_{max}(N = 1) \approx 17°$ for the strongest longitudinal field considered which is a reduction by more than 50% (Figure 11). The corresponding path deviates less from the vertical direction as shown in Figure 12. A zig-zag trajectory is found for all values of N considered, with the transverse distance between two extreme points being reduced with increasing the strength of the magnetic field. The time scale for one zig-zag increases as well, i.e. the path oscillation is stretched in the direction of gravity. At the same time the amplitude of the oscillations is somewhat smaller, as shown in Figure 12 and Table 3. The resulting 3D bubble trajectory is therefore more rectilinear. The amplitude of the oscillation in $Re(t)$ decreases with N and the bubble rises faster (Figure 10). The time-averaged rise Reynolds number increases by about 8% for the largest field. The oscillation in $Re(t)$ appears more regular in the case with $N = 0.5$ and even more for $N = 1$ compared to the case without magnetic field.

3.3. Comparison of results with experimental data and interpretation

A comparison with the experimental data from [22] is provided in Figure 13 and Figure 14. Here, the average rise Reynolds number and the Strouhal number are normalized with the value in the absence of a magnetic field ($N = 0$) and are plotted over the magnetic interaction parameter N for different Eötvös numbers Eo, reflecting different bubble sizes.

3.3.1. Time-averaged Reynolds number versus N and Eo

Whether the time-averaged rise velocity decreases or increases with increasing magnetic interaction depends on the bubble size. This complex behavior is found in both, the present simulations and the experiments in the literature [22]. An increase in rise velocity and hence Re_t with increasing magnetic field is found for large bubbles, i.e. large Eo, and a decrease in Re_t for small bubbles, i.e. small Eo. The reason for this phenomenon is a competition between adverse effects generated by the magnetic field: On the one hand, a longitudinal magnetic field increases the drag of an object. In order to pass around the object fluid elements need to move in a direction perpendicular to the magnetic field which generates a Lorentz force such that the resulting pressure force on the particle increases with magnetic interaction. This was shown experimentally for the flow around a fixed sphere and a disc at high Reynolds number and moderate to high magnetic interaction [30, 51] as well as numerically for spheres and ellipsoids at moderate Re in [52]. On the other hand, the magnetic field suppresses the lateral dynamics and the bubble rises on a more rectilinear trajectory. Already in the inviscid situation this leads to a larger rise velocity, simply because the trajectory is shorter. Considering viscous effects in addition, less energy is transferred towards rotation and towards motion in the transverse direction where it is dissipated further increasing the rise velocity. The amplitude of the changes in $|Re_t(N)/Re_t(N=0)|$ with N lies well within the band spanned by the data obtained from the experiments. The measurements, however, show a different threshold in Eo for the reversion of the trend, i.e. Re_t increases or decreases with N at slightly larger Eötvös numbers. This is visualized in Figure 13.

3.3.2. Frequency versus N and Eo

Different ways of defining a non-dimensional frequency have been proposed in the literature so that before reporting the results obtained a few comments on this issue are appropriate. The equivalent bubble diameter d_{eq} is a natural reference length in any case. But one can either choose the *a posteriori* determined time-average rise-velocity $\langle v_p \rangle_t$ or the *a priori* known gravitational velocity scale $u_{ref} = \sqrt{|\pi_\rho - 1| d_{eq} g}$ to determine a reference time scale. As in the experiments [22], the Strouhal number

$$St = \frac{f^* \, d_{eq}}{\langle v_p \rangle_t} \tag{10}$$

is employed here which is based on the dominant frequency f^* in the oscillation of the vertical bubble velocity $v_p(t)$ and on the average rise velocity $\langle v_p \rangle_t$ of the bubble. The average rise velocity itself is a function of bubble size and magnetic interaction. In contrast, the dimensionless frequency $f_{Re} = f^*/f_{ref} = f^* \, d_{eq}/u_{ref} = f^*/\sqrt{|\pi_\rho - 1| \, g/d_{eq}}$ is based on the constant reference velocity given by the gravitational velocity scale. Therefore the Strouhal number according to (10) measures the combined effect of an additional parameter on both, the average velocity and the frequency in the velocity oscillations.

The determination of St and f_{Re} can only be based on a small number of periods of the oscillation in $Re(t)$ here due to the size of the computational domain. The number of periods observed in the experiments is the same for $N > 0$. A decrease of the bubble Strouhal number St and of f_{Re} is found with increasing strength of the magnetic field for all bubble sizes. The relative change in St is less pronounced for small bubbles than for large bubbles in the simulation. For the larger bubble with $Eo = 2.5$, the reduction in St is over-predicted at large magnetic interaction parameters in the simulations. To quantify the influence of spatial resolution on the result, 'coarse' simulations with an isotropic grid of step size 1.5 times the one of the common grid, i.e. $n_x = 192$, have been conducted for this bubble using the same values of the interaction parameter $N = 0,\ 0.5,\ 1.0$. It appears that the results for the relative change in St on the finer grid are closer to the experimental data.

Overall, the agreement of the results of experiments and numerical simulations is promising. All dominant effects of the magnetic field have been captured by the simulation.

3.4. Comparative analysis of wake with and without magnetic field

3.4.1. Selection of characteristic events in the trajectory

For the bubble with $G = 2825$, $Eo = 2.5$, three particular instants in time, A, B, C, are chosen for further analysis. These events correspond to characteristic points in the bubble trajectory, extreme points of bubble inclination $\phi_z(t)$ and path $x_p(t)$, and are illustrated in Figure 6 and highlighted as dots in Figures 15. The inclination $\phi_z(t)$ is zero for event A and C. The time of event B was chosen half way between the time of A and C corresponding to approximately an extremum in inclination $\phi_z(t)$. Events A and C mark approximately the turning points of the zig-zag in $x_p(t)$. We therefore restrict the discussion to half a period of the zig-zag. At instant B, the transverse velocity u_p is close to a maximum and the instantaneous rise Reynolds number $Re = v_p d_{eq}/\nu$ just passed a minimum (Figure 15c).

3.4.2. Coherent structures in the wake

As discussed in the introduction, the trajectory of the bubble is closely related to the structure of its wake. In experiments with liquid metal, an analysis of coherent vortex structures is difficult. The presently available experimental techniques only provide selected one- or two-dimensional data with relatively coarse resolution [22, 16, 53, 54]. Here, the present simulations can close this gap and furnish insight into vortical structures of the bubble wake. This is provided in Figures 16 to 18 based on instantaneous 3D velocity and pressure data available from the simulations. The dominant role of streamwise vorticity has been emphasized by several others, for instance in [4, 13, 2]. Figure 16 and 17 for this reason show the vertical component of the vorticity, ω_y, for event B and C, respectively. Two iso-surfaces are depicted, one with a positive and one with a negative value, so that counter-rotating vortices can be detected. In these plots, complementary views of the same structure are shown differing by an angle of 90°. The magnetic interaction parameter increases from left to right from $N = 0$ to $N = 0.5$ to $N = 1.0$.

Visualizations using the λ_2-criterion [55] were conducted as well. These are not reproduced here since they show very much the same structures as the vorticity plots, at the same level of granularity. The vorticity in the wake is distributed in an undulating pattern as a consequence of two effects. One is the von Kármán instability of the wake leading to an alternating vortex pattern even if the bubble would rise along a straight path. Additionally, once the path of the bubble oscillates in horizontal direction, vorticity is generated at varying horizontal positions, so that even without the wake instability a zig-zag trajectory yields a zig-zag shape of the vorticity pattern. Also recall that in inviscid smooth fluid flows, vortex lines move with the fluid [56]. In all cases, one can observe that vorticity is shed pair-wise with alternating sign in the zy-plane. These counter-rotating vortex filaments induce a velocity in the x-direction according to the Biot-Savart law yielding a tilting of the bubble and hence the observed zig-zag motion in the xy-plane. Substantial damping of the vortical structures in the bubble wake by the vertical magnetic field is found. Especially small structures vanish with increasing N while the larger vortex filaments are more aligned with the field. The vertical orientation of the vortices, in turn, is also caused by the more rectilinear trajectory of the bubble.

While iso-contours of the vertical vorticity component give access to coherent structures of smaller scales, iso-contours of pressure can be used to visualize larger scales [57]. As vortex cores are characterized by low pressure regions, iso-contours of the pressure coefficient $C_p = p \,/\, \left(\rho_f u_{ref}^2/2\right)$ are displayed in Figure 18 for event C. (Recall that the hydrostatic component of the pressure has been subtracted from the equations.)

Vortex rings form in the wake of the bubble in the absence of a magnetic field triggered by the zig-zag path which have also been visualized in experiments at similar Reynolds number [8]. A $4R$ vortex mode [8] is associated with one zig-zag period consisting of two primary vortex rings at the extreme points of the path and two secondary rings in between at maximum, absolute inclination. These rings are less pronounced in the case $N = 0.5$ and eventually vanish for $N = 1.0$ due to the rather rectilinear path. The 'two-legged' structure of the bubble wake is clearly visible in the snapshot of $N = 0.5$ at the chosen value for C_p.

The pressure iso-contours also show a region of high pressure at the front of the bubble and a low pressure region aside from and behind the bubble. Both regions increase in size with increasing magnetic interaction indicating an augmentation of the pressure drag on the bubble with N as discussed in [30]. The Lorentz force is generated by the transverse velocity components u and w

for a vertical magnetic field, so that increasing magnetic interaction leads to a damping of these lateral velocity components and to a straightening and stretching of the path lines of fluid elements around the bubble in vertical direction resulting in the described change in the pressure field. The effect is also visible in the graphs of Figure 19 where the extent of non-zero transverse vorticity in front of the bubble increases with stronger magnetic fields.

3.5. Quantification of the damping effect in the bubble wake

The vorticity in the bubble wake has been found to be the crucial quantity in understanding bubble dynamics and path oscillations [13, 2, 4]. Therefore, the focus is now on the quantification of the damping effect resulting from the applied magnetic field. The absolute value of the vorticity component ω_y is integrated in xz-planes according to

$$\langle|\omega_y|\rangle_{xz} = \frac{1}{d_{eq}^2} \iint \frac{|\omega_y|}{\omega_{ref}} \, dx \, dz \, . \tag{11}$$

The integration in equation (11) is conducted over the entire xz-plane and normalized with d_{eq}^2 and $\omega_{ref} = u_{ref}/d_{eq}$. The transverse components $\langle|\omega_x|\rangle_{xz}$ and $\langle|\omega_z|\rangle_{xz}$ are determined in an analogous way.

Sample results for event C are plotted over the vertical distance from the bubble center for increasing magnetic interaction $N = 0,\ 0.5,\ 1.0$ in Figure 19. The plots show global maximum values of $\langle|\omega_x|\rangle_{xz}$ and $\langle|\omega_z|\rangle_{xz}$ at the front of the bubble in all cases. The values of the maxima are similar since the bubble has zero tilting at event C and therefore the geometrical configuration is symmetric with respect to x and z at this instant in time. With increasing magnetic interaction the maximum in $\langle|\omega_x|\rangle_{xz}$ and $\langle|\omega_z|\rangle_{xz}$ is reduced and the region of non-zero vorticity extends further upstream. In the bubble wake, considerable damping of all vorticity components is found when a magnetic field is applied. The peaks of $\langle|\omega_y|\rangle_{xz}$ for $N = 0$ in Figure 19a vary in amplitude due to asymmetries in the zig-zag and tilting of the bubble as well as due to irregular vortex shedding. With increasing magnetic interaction, the bubble wake contains less vertical vorticity and the values of the extrema in the plot are substantially reduced.

The damping effect of a vertical magnetic field is anisotropic. Joule damping associated with the Lorentz force acts linearly on all scales with a privileged direction [28]. This is now assessed by means of the average weight of $|\omega_y|$ compared to the total vorticity $|\boldsymbol{\omega}|$ using the quantity

$$\Gamma_y = \frac{1}{n_{xz}} \sum_{i=1}^{n_{xz}} \frac{\langle|\omega_y|\rangle_{xz}^{(i)}}{\langle|\boldsymbol{\omega}|\rangle_{xz}^{(i)}} \, . \tag{12}$$

With the present data, $n_{xz} = 1280$ equi-distributed xz-planes have been used for the interval $(y_p - y)/d_{eq} \in [-5; 25]$. The quantity Γ_y is reported in Table 4 for event C. The table also lists an integral measure of vorticity for all three components obtained by summation over all xz-planes. The difference in the damping of ω_x and ω_z is related to the privileged direction of the zig-zag. A roughly linear decrease of Γ_y with N is found, i.e. the vorticity component ω_y is the one which is affected most by the magnetic field. In general, a vertical magnetic field leads to homogenization of the transverse velocities u and w and therefore reduces the gradients of these components with respect to z and x which enter in ω_y.

In summary, the applied vertical magnetic field particularly reduces the transverse velocities u and w and therefore indirectly the vertical component of the vorticity ω_y. This streamwise vorticity is the direct cause of the zig-zag trajectory which is consequently reduced when ω_y is smaller.

3.5.1. Energy spectra

Using the simulation data, energy spectra were obtained for the velocity components v and u, corresponding to the direction of ascent and the predominant direction of the zig-zag, respectively. These spectra are spatial spectra and were determined along vertical lines through the bubble center (x_p, z_p) and along additional vertical lines shifted by $\pm r_{eq}$ in x and z.. The spectra resulting from these five lines were ensemble-averaged, as well as time-averaged in an interval of $\Delta t_{\langle\,\rangle} = 1.25$ around event C. A byproduct of the immersed boundary method applied here is an artificial, weak flow field inside the bubble [32]. The velocity field therefore is continuously differentiable in the entire domain and sampling data through the bubble does not effect the convergence of the spectra. The spectra E_{vv} and E_{uu} are shown in Figure 20 over the spatial wave number ξ_y for the case without magnetic field, $N = 0$, and the strongest vertical magnetic field applied, $N = 1$. The results for $N = 0.5$ lie in between and have been removed for readability.

For $N = 0$, the spectrum of u exhibits an increase with wave number for small ξ_y, a maximum, and a regular decay over more than two decades. Beyond this, a fine-scale range with steeper decay is observed. The spectrum of the vertical velocity component behaves similarly. The overall amplitude is larger, particularly for the lower wave numbers, as this component is in the direction of the bubble rise velocity. Again, the high-frequency end of the spectrum decays fast and does not exhibit any sign of unphysical behavior as it would occur from under-resolution due to aliasing, etc. On the other hand, it can not be excluded that the finest scales are influenced by the grid resolution.

In addition to the grid study presented above, the regular decay in both spectra over a large range of wave numbers demonstrates that the flow indeed is well resolved in its energy-containing range and well beyond.

The second type of information which can be extracted from Figure 20 relates to the application of the vertical magnetic field. It is apparent that the u-component, which is perpendicular to the field, is damped by an almost constant factor in the entire mid-to-high-frequency range. The amplitudes of the large wave numbers are also uniformly damped, but by a somewhat smaller factor. For the vertical component, a similar observation is made, except for the low wave numbers where the slope of the spectrum is changed. As a result, the largest scales are less influenced by the magnetic field. Overall, the damping by the magnetic field is seen to be stronger in the spectrum of u compared to the spectrum of v. This is coherent with the understanding of the action of the Lorentz force affecting predominantly the velocity component perpendicular to the field as discussed above. The spectra are instructive in this respect as they reveal damping, albeit less, also for the v-component of the velocity.

3.6. Examination of the employed numerical modeling

The scope of this section is to scrutinize the assumptions employed in the numerical modeling, and also to provide a comparative view on the experimental data for the ascent of a single argon bubble in the liquid metal GaInSn. With the numerical model described above, already a very good agreement with the experimental data was achieved in the previous sections. All dominant effects of the magnetic field observed in the experiments were reproduced, and could be analyzed in more depth based on the available computational data of high detail. However, there is still room for improvement in the quantitative agreement. Furthermore, awareness of possible sources of error is important and an estimate about the magnitude of the error is a valuable information. Therefore, the influence of the bubble shape representation is studied now and the impact of the insulating bubble on the distribution of the electric current density is examined.

3.6.1. Influence of bubble shape representation

So far the bubble shape was approximated as an oblate ellipsoid where the ellipsoid aspect ratio was correlated to the instantaneous bubble Weber number, $X(t) = f(We(t))$. The wake instability of a fixed axisymmetric bubble of realistic shape [58], however, shows a perceptible difference with respect to the instability of a bubble with oblate ellipsoidal shape [12]. Consequently, an additional

simulation is conducted without magnetic field and the bubble shape represented by axisymmetric spherical harmonics (SH) up to a polynomial degree of $N_{SH} = 12$. The shape is computed directly from the local fluid load along the bubble surface by the SH shape algorithm described in [38]. All other parameters of the simulation remain unchanged. The non-dimensional numbers describing the simulation are $G = 2825$, $Eo = 2.5$, $N = 0$, i.e. no magnetic field is applied.
Figure 21 shows the bubble aspect ratio over time as well as the time-averaged bubble shape for both runs. The average shapes are nearly identical whereas the SH bubble has a moderate front-aft asymmetry being a bit front-flattened. In the case of the SH bubble, the aspect ratio is computed from $X = 2\max(x')/(\max(y')-\min(y'))$ which results in a slightly lower value for the time-averaged aspect ratio. In the definition of the aspect ratio, x' and y' are points on the bubble surface in the local reference frame of the bubble with y' being collinear to the axis of rotation of the SH and x' perpendicular to it. The projected area of the bubble during the ascent is however very much the same for both shape representations. Also the amplitude and frequency in the shape oscillation agree very well. Table 22a) lists the main figures describing the bubble dynamics and compares the results obtained with an ellipsoidal bubble shape, the SH representation, and the experimental data. Figure 22b) again shows the history of the bubble rise Reynolds number for the three cases. With the SH shape representation, a slightly higher average rise Reynolds number, Re_t, is observed compared to the ellipsoidal shape. The standard deviation, σ_{Re}, increases noticeably towards the experimental value whereas the frequency, f_{Re}, in the oscillation remains almost unchanged. The maximum inclination, $|\phi_z|_{max}$, decreases somewhat to 32°, while the measure of the zig-zag, Δ_{xz}/d_{eq}, is basically unaltered.

In summary, the approximation of the bubble shape as an oblate ellipsoid was well justified in the present case. The more sophisticated approach with the bubble shape represented by spherical harmonics and coupled to the hydrodynamic forces yields a very similar bubble shape and well comparable bubble dynamics. A non-axisymmetric shape might further improve the results. The correlation of the bubble aspect ratio to the instantaneous Weber number did also yield good agreement for the bubble shape oscillation. The additional simulation provides an *a posteriori* justification of the previous assumptions towards the bubble shape.

3.6.2. Influence of the electrically insulating bubble

One assumptions made above is to set the electric conductivity inside the bubble the same as in the liquid. In this section, the bubble is treated as a local insulator. The representation of internal electric boundary conditions can be achieved by a magnetohydrodynamic IBM [59]. With this approach, an IBM correction is introduced to Ohm's law (3) in the vicinity of the non-conducting immersed surface, S, to ensure $\mathbf{j}_S = 0$ [59]. In a very similar fashion, we here impose zero electric current inside the entire bubble by a phase-dependent conductivity, $\sigma_e(\alpha)$, with $\alpha = 1$ inside the bubble and $\sigma_e(\alpha = 1) = 0$ [33]. The phase-indicator, $\alpha \in [0, 1]$, is obtained from a second-order accurate level-set approach [41]. With the modified numerical modeling, the electric current cannot penetrate the phase boundary and the current circuits have to close through the liquid metal.

A one-to-one comparison with the above results again using the ellipsoidal shape is not conducted here, because the simulations are quite expensive. Instead the bubble shape is represented by spherical harmonics to achieve as much improvement as possible. All other parameters remain as outlined above. The study is further extended towards larger magnetic interaction parameters.

Figure 23 shows an instantaneous contour of the current density component, j_z. Note that this plot provides information about the Lorentz force component, $f_{L,x}$ at the same time, since the Lorentz force is $f_L = 1/\rho_f \, \mathbf{j} \times \mathbf{B}$ and thus $f_{L,x} \sim -j_z$ for a vertical homogeneous magnetic field. The non-dimensional numbers describing the simulation are $G = 2825$, $Eo = 2.5$, $N = 1$. Here, Figure 23a) shows a contour with ellipsoidal bubble shape and $\sigma_e = const.$, while Figure 23b) displays a similar instant for a non-conducting bubble and its shape represented by spherical harmonics. The close-up Figure 23c) shows a detailed view of the phase boundary and the mesh for case b). With the present configuration, the current distribution is very similar for both cases even in the direct vicinity of the bubble. The current streamlines have to close due to charge conservation which leads to the formation of circular patterns in front of the bubble and distorted loops in the bubble wake as depicted in Figure 23. The corresponding Lorentz force distribution introduces damping of the transverse velocity components and indirectly affects the rise velocity, e.g. by altering the pressure field around the bubble.

Table 5 summarizes the main results for the insulating bubble with SH bubble shape for various magnetic interaction parameters. The numbers in brackets indicate the previous simulation results with ellipsoidal bubble shape and constant electric conductivity. For $N = 1$, the average rise Reynolds number, Re_t, is almost identical for the insulating bubble with SH bubble shape compared to the value obtained when imposing an ellipsoidal shape and determining the aspect ratio from the instantaneous bubble velocity and constant electric conductivity. The relative decrease in the standard deviation, σ_{Re}, compared to the case without magnetic field is similar for both runs with larger absolute values in the simulation with the insulating bubble. The most significant change is that there is a less pronounced damping in the dominant frequency, f_{Re}, in the case of an insulating bubble. Now excellent agreement with the experimental data is found for the damping in the bubble Strouhal number. At a value $N = 1$ of the interaction parameter, the decrease in Strouhal number is $St/St(N = 0) = 0.775$, while the value calculated from the experimental data is 0.779 so that the agreement is very good. With constant electric conductivity and ellipsoidal shape, the relative change in Strouhal number was $St/St(N = 0) = 0.656$. In each case, the reference values taken for $N = 0$ were obtained with the corresponding shape representation.

The extension of the study towards larger values of N supports the physical explanation of the effects of a longitudinal magnetic field on the bubble dynamics given in the previous sections. Indeed, there is a local maximum in Re_t over N for larger bubbles. Further increasing the magnetic interaction, the drag increases and the bubble rises slower. This is in agreement with the observation of a monotonously increasing drag with N for the flow around a fixed sphere or ellipsoid observed in [30, 51]. The local increase in Re_t for low and moderate N stems from the damping of the lateral dynamics and the more rectilinear trajectory compared to the case without magnetic field. A roughly linear decrease in the bubble Strouhal number with N is observed for small to moderate interaction parameters which then seems to saturate at $N = 4$ where the damping is less pronounced. Note that the statistics for the simulation with $N = 4$ were obtained for two crossings of the periodic domain, but still only three quasi-periods of the oscillation in $Re(t)$ could be used. The uncertainty in the frequency and standard deviation of the oscillation therefore is rather high. For values of the magnetic interaction parameters studied here, the lateral dynamics of the high Reynolds bubble were not fully suppressed by the magnetic field.

In summary, using an insulating bubble does improve the quantitative agreement with the experiments. The effect of the longitudinal magnetic field on the bubble dynamics, however, remains the same as in the studies reported above. With the improved modeling, further simulations at higher magnetic interaction were conducted and the physical explanations on the impact of the field on the rise Reynolds number are supported.

4. Conclusions

Phase-resolving simulations of single bubbles rising in liquid metal were conducted in this paper. The following effects are observed when increasing the magnetic interaction parameter N compared to the case without magnetic field:

The time-averaged bubble rise velocity increases for large bubbles (high Eo) reaches a local maximum and then decreases. For small bubbles (low Eo), the time-averaged bubble rise velocity decreases for all N studied. The amplitude of oscillations in $v_p(t)$ decreases. The dimensionless characteristic frequency f of oscillations in $Re(t)$ and the resulting Strouhal number St decrease for all bubbles. The amplitude of oscillation in lateral bubble positions $x_p(t)$, $z_p(t)$ decreases, i.e. the trajectory is more rectilinear. Also the amplitude of oscillation in tilting angles $\phi_i(t)$ decreases. The integral of the absolute value of the vertical vorticity component over cross sectional planes in the bubble wake decreases. Similar observations were made for the transverse components, but the vertical component of vorticity is affected most by the damping due to the vertical magnetic field. The obtained results are in good agreement with the corresponding experiments presented in [22]. The present results for the instantaneous vertical bubble and fluid velocity support the findings from these experiments where the velocity component along a line was measured by ultrasound Doppler velocimetry. Furthermore, additional data are now available from the simulations elucidating the full three-dimensional bubble trajectory, flow structures in the bubble wake and wake vorticity as well as energy spectra. These data provide valuable insight into the considered three-dimensional multiphase flow and into the dynamics of a single bubble in liquid metal under the impact of a longitudinal magnetic field which can so far not be obtained by experiments.

Future research will be concerned with the simulation of bubble chains and bubble swarms in liquid metal to provide insight into the influence of a magnetic field on collective effects in bubble driven flows [16, 60]. Another interesting direction of research is the influence of a magnetic field on the flow through a relatively tight cluster of bubbles as presented in [33, 61]

Acknowledgments

The present work was partly funded by DFG in the framework of SFB 609. Computing time was provided by ZIH, Dresden. The authors like to thank S. Eckert and C. Zhang, HZDR, Dresden for interesting discussions on the topic and for providing their experimental data in electronic form.

5. Figures and captions

Table 1. Material properties of GaInSn and water at a temperature of $20°C$ and ambient pressure of 1 bar [22]. The non-dimensional numbers are calculated for an argon bubble in GaInSn and an air bubble in water, both with an equivalent diameter of $d_{eq} = 4.6$ mm.

	GaInSn	Water
Density ρ_f $[kg\, m^{-3}]$	6361	998
Surface tension σ $[N\, m^{-1}]$	0.533	0.073
Kinematic viscosity ν $[m^2\, s^{-1}]$	$3.46 \cdot 10^{-7}$	$9.82 \cdot 10^{-7}$
Electrical conductivity σ_e $[S\, m^{-1}]$	$3.27 \cdot 10^{6}$	$\approx 5.0 \cdot 10^{-2}$
Galilei number G	2825	995
Eötvös number Eo	2.5	2.8

a) b)

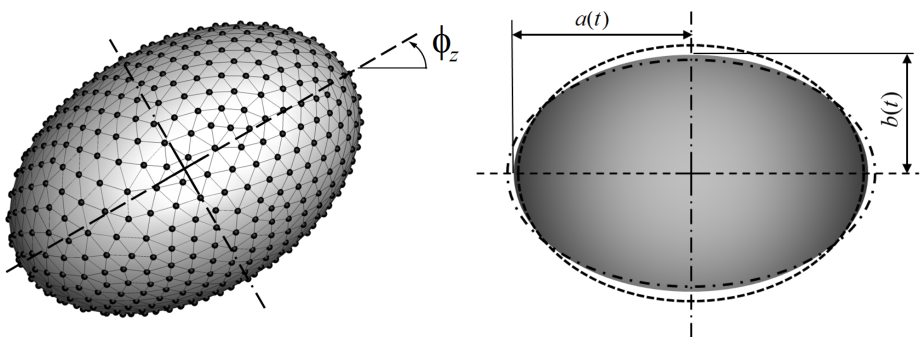

Figure 1: a) Ellipsoidal bubble with $n_L = 664$ Lagrangian forcing points, tilted by $\phi_z = 30°$. b) Shape oscillation $X(t) = a(t)/b(t)$. The discontinuous lines indicate the states with maximum and minimum aspect ratio observed in the simulation with $N = 0$ reported below.

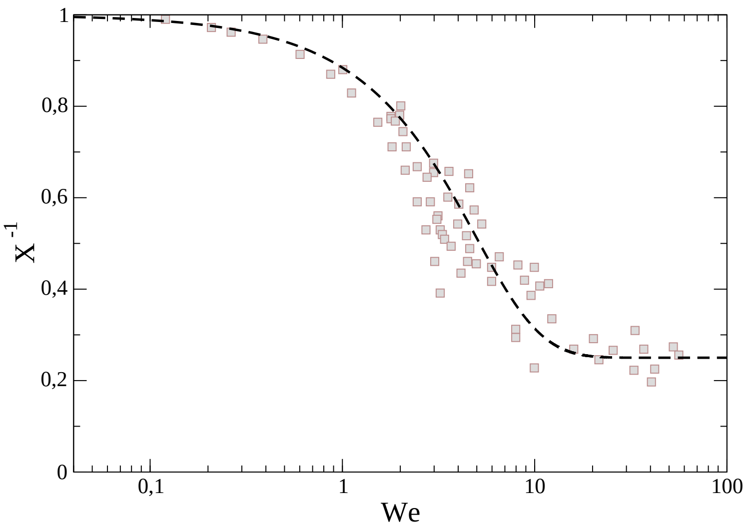

Figure 2: Bubble shape: Aspect ratio X over Weber number We, data (symbols) and fit from [20].

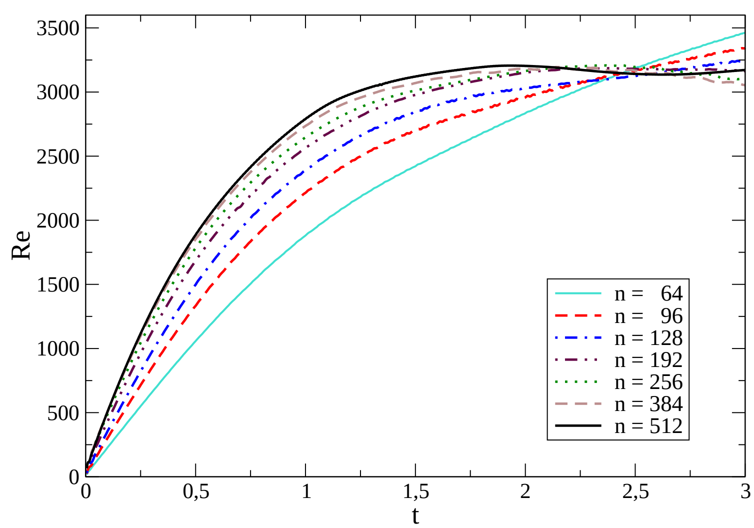

Figure 3: Bubble Reynolds number over time as a function of grid spacing, $N = 0$.

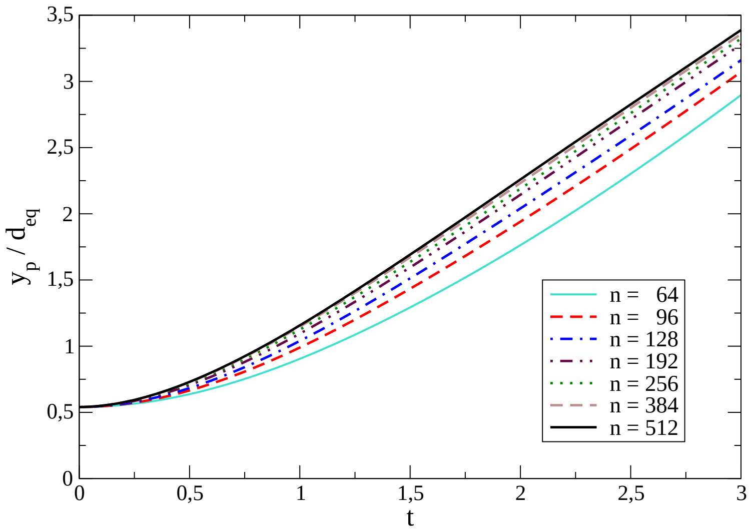

Figure 4: Vertical position of the bubble over time as a function of grid spacing, $N = 0$.

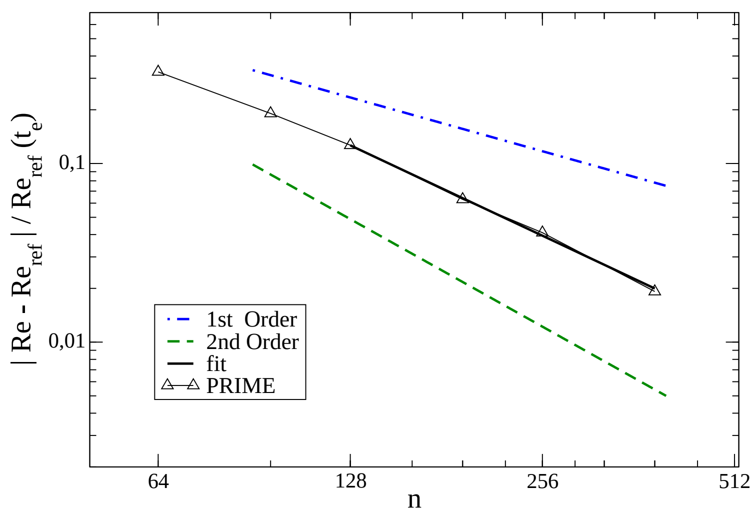

Figure 5: Relative error in Re at $t = 1.0$ for the simulation in Figure 3.

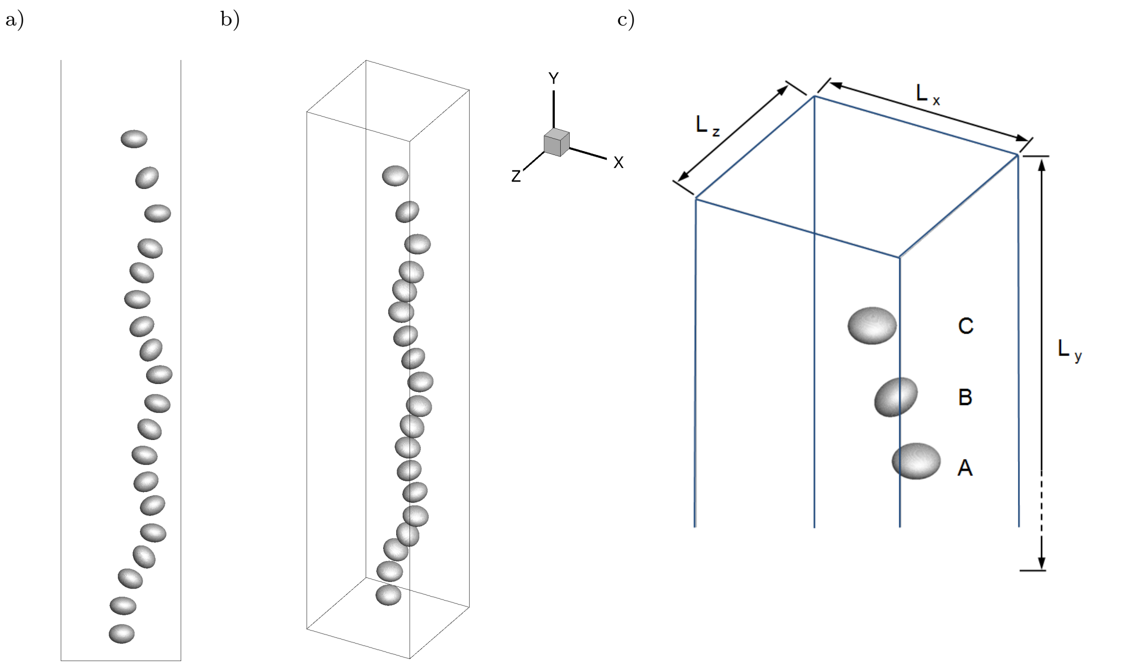

Figure 6: a) Side view of computational domain and bubble trajectory for $N = 0$ and b) perspective view of the same data, c) events A, B, C of the bubble trajectory for this case as indicated in Figure 15 below.

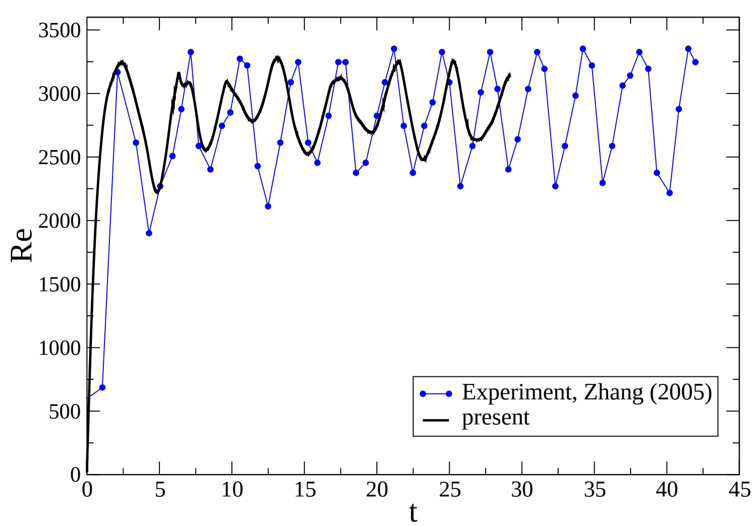

Figure 7: Bubble Reynolds number over time for $N = 0$ and comparison to experimental data of [22].

Table 2. Results for a single bubble without magnetic field compared to experimental data of [22]. $Re_t = \langle Re \rangle_t$ is the temporally averaged Reynolds number, σ_{Re} the corresponding standard deviation, $f_{Re} = f^*/f_{ref}$ with f^* being the dominant frequency in Hz and $f_{ref} = \sqrt{|\pi_\rho - 1|\, g/d_{eq}}$.

	Re_t	σ_{Re}	f_{Re} (DFT)	f_{Re} (roots)	f_{Re} (sine-fit [22])
Simulation	2871	245	0.276	0.270	—
Experiment [22]	2879	369	0.297	0.289	0.280

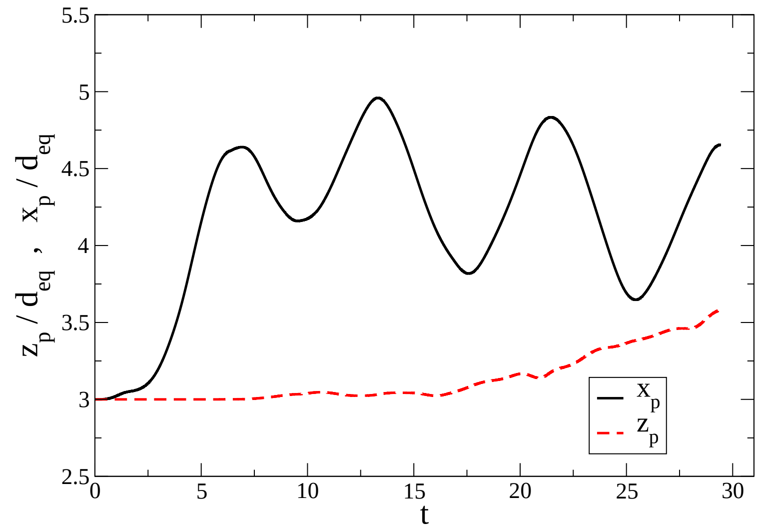

Figure 8: Zig-zag trajectory for $N = 0$. History of lateral bubble center coordinates x_p and z_p, non-dimensionalized with d_{eq}.

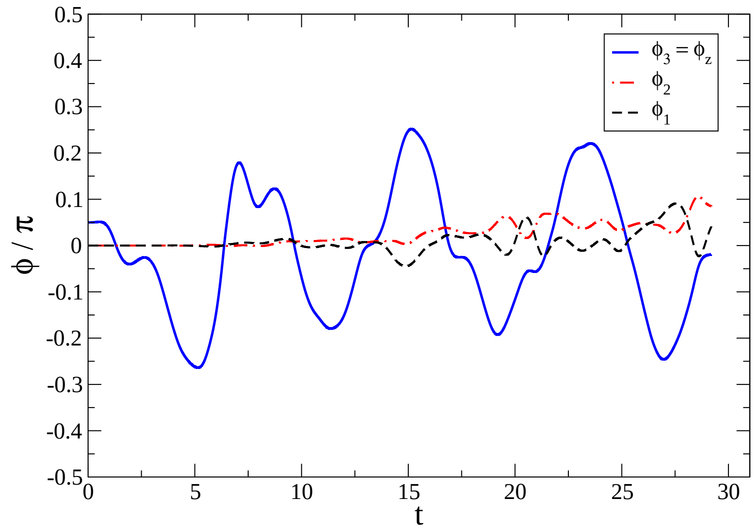

Figure 9: Bubble orientation over time for $N = 0$ described by the angles of orientation.

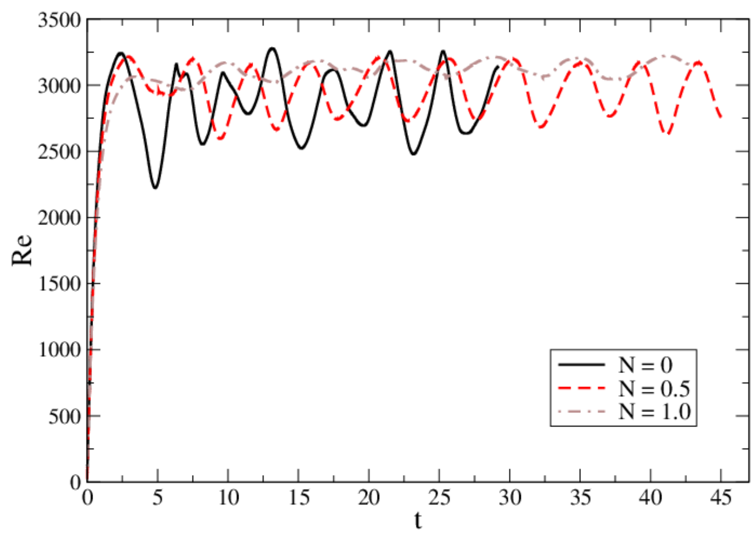

Figure 10: History of bubble Reynolds number for the three cases $N = 0,\ 0.5,\ 1.0$ and $G = 2825$, $Eo = 2.5$.

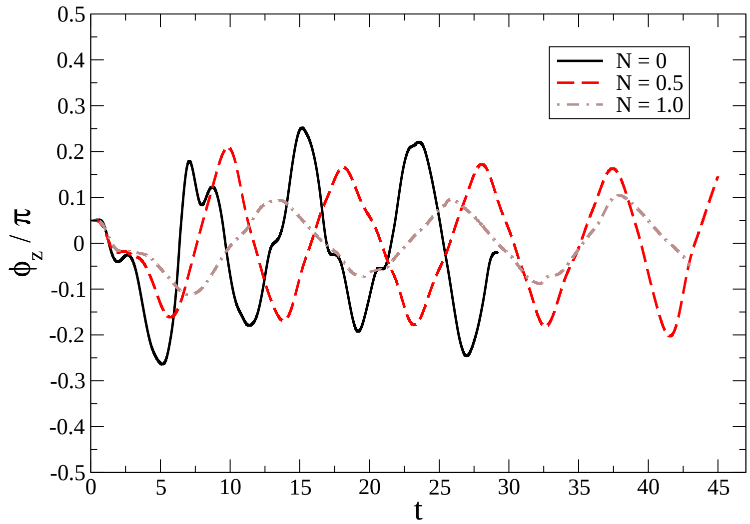

Figure 11: History of inclination angle ϕ_z for the three cases $N = 0,\ 0.5,\ 1.0$ and $G = 2825$, $Eo = 2.5$.

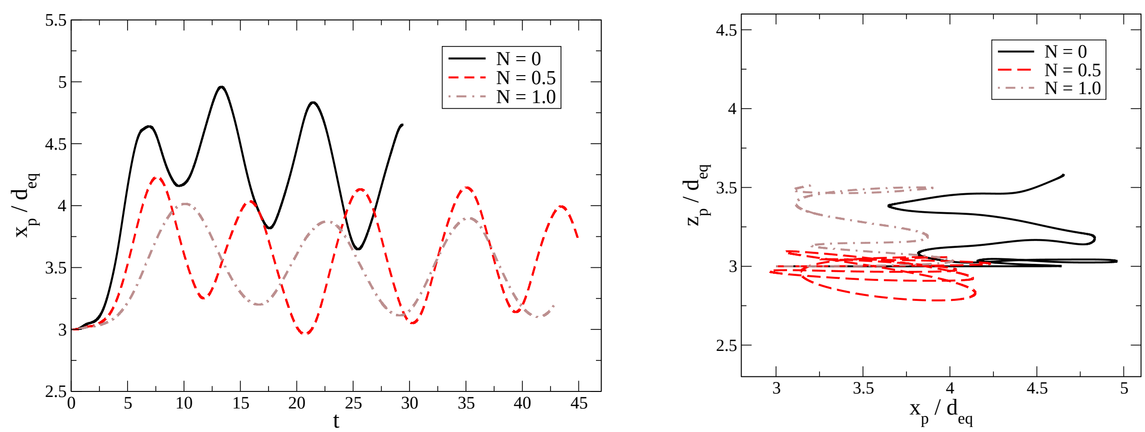

Figure 12: Assessment of lateral motion with and without magnetic field. $N = 0,\ 0.5,\ 1.0$ and $G = 2825$, $Eo = 2.5$. Left: History of lateral bubble center coordinates x_p non-dimensionalized with d_{eq} illustrating the zig-zag trajectory of the bubble. Right: Top view on trajectories, x_p versus z_p, only the center part of the domain is shown.

Table 3. Summary of simulation results.

$Eo = 2.5$, $G = 2825$, fine	Re_t	f (DFT)	$\|\phi_z\|_{max}$	Δ_{xz}(Zig-Zag)
$N = 0$	2871	0.276	36°	$1.15\, d_{eq}$
$N = 0.5$	2957	0.233	31°	$1.08\, d_{eq}$
$N = 1.0$	3132	0.181	17°	$0.78\, d_{eq}$
$Eo = 2.5$, $G = 2825$, coarse				
$N = 0$	3029	0.297	35°	$0.96\, d_{eq}$
$N = 0.5$	3054	0.246	29°	$0.92\, d_{eq}$
$N = 1.0$	3202	0.185	15°	$0.73\, d_{eq}$

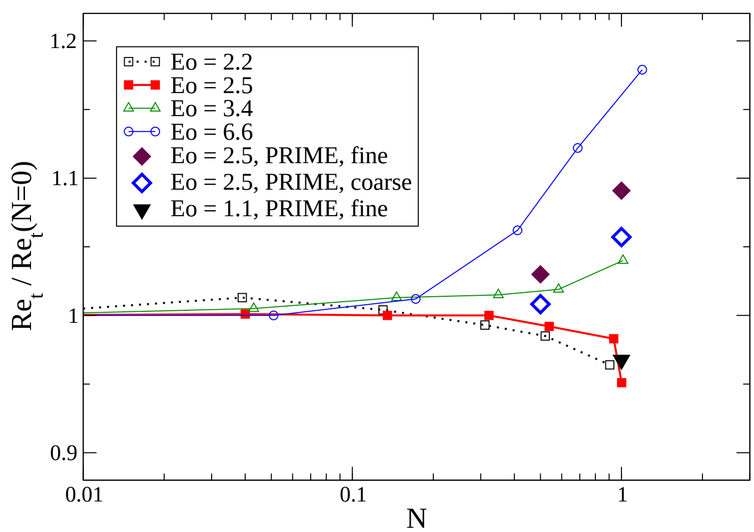

Figure 13: Relative change in average rise Reynolds number: Present simulations (bold symbols) with code PRIME compared to experimental data of [22].

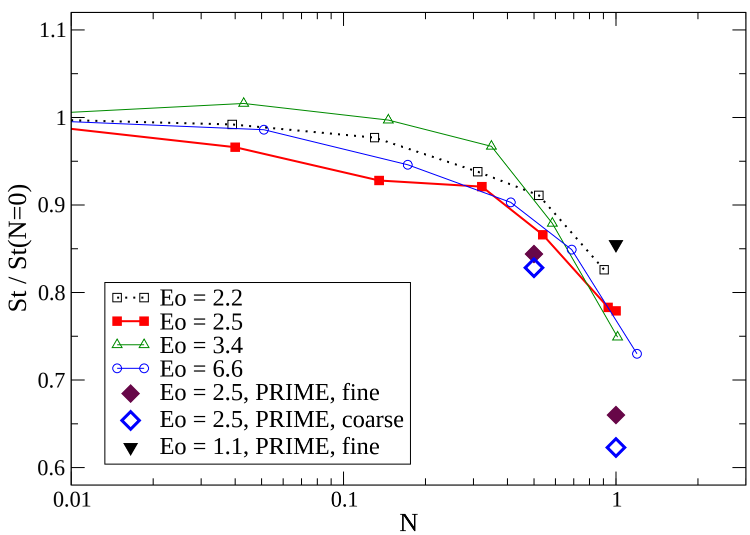

Figure 14: Relative change in Strouhal number: Present simulations with code PRIME compared to experimental data of [22].

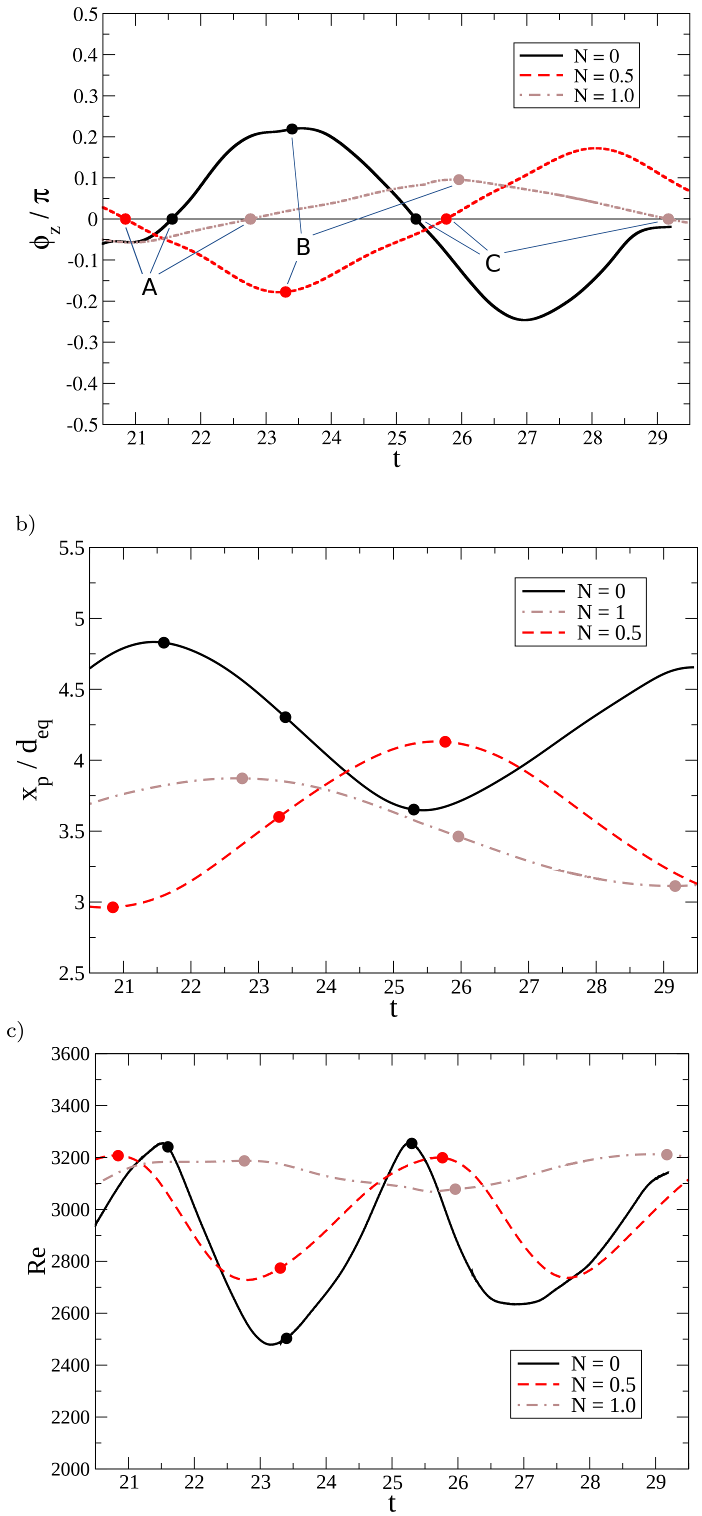

Figure 15: Selected instants in time A, B, C characteristic for the bubble trajectory. They are defined in the plot of the inclination angle ϕ_z and marked by dots in the other plots of bubble position x_p and bubble Reynolds number for the three cases $N = 0,\ 0.5,\ 1.0$; $G = 2825$, $Eo = 2.5$ in all cases.

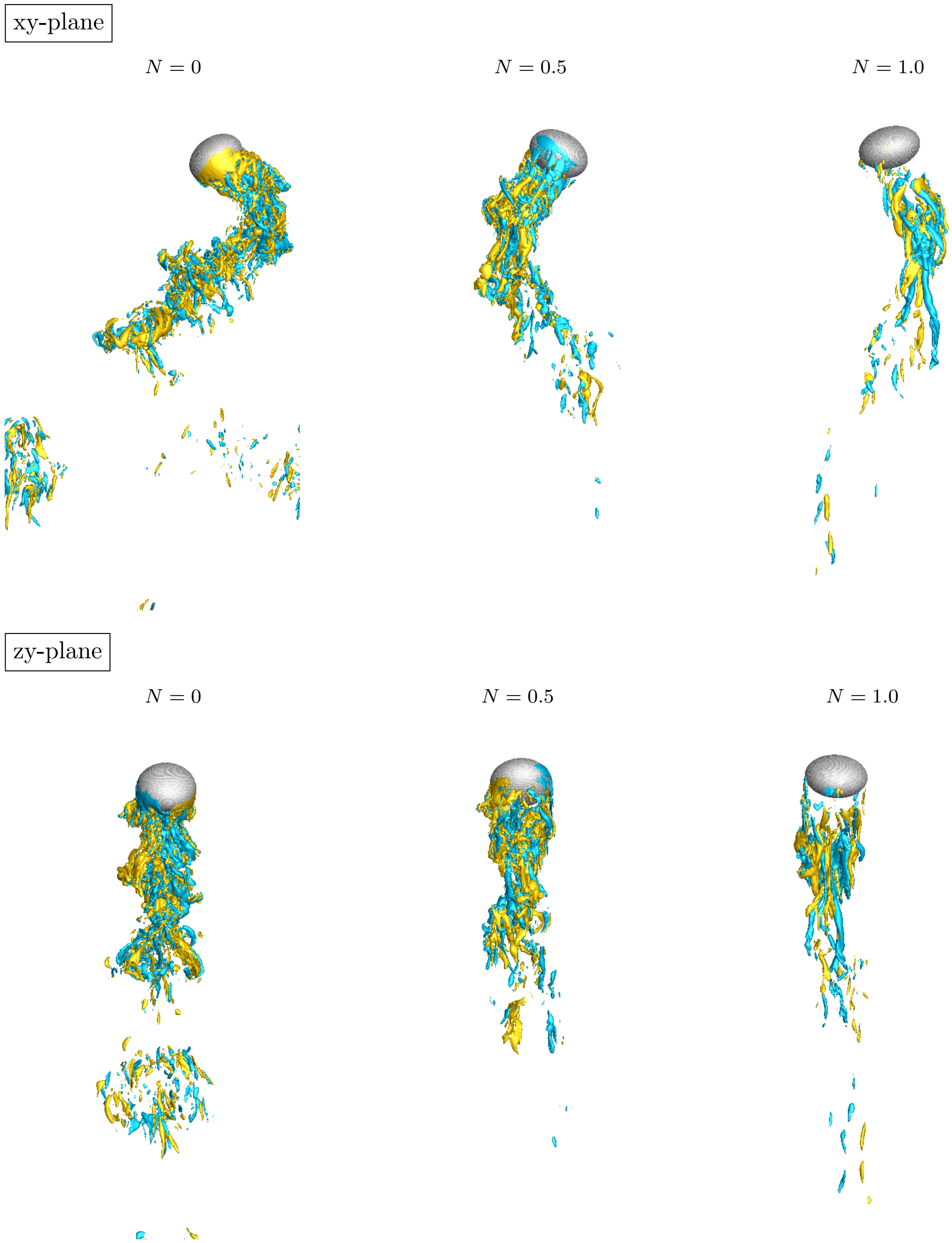

Figure 16: Event B: Iso-contours of $\omega_y d_{eq}/u_{ref} = \pm 6$.

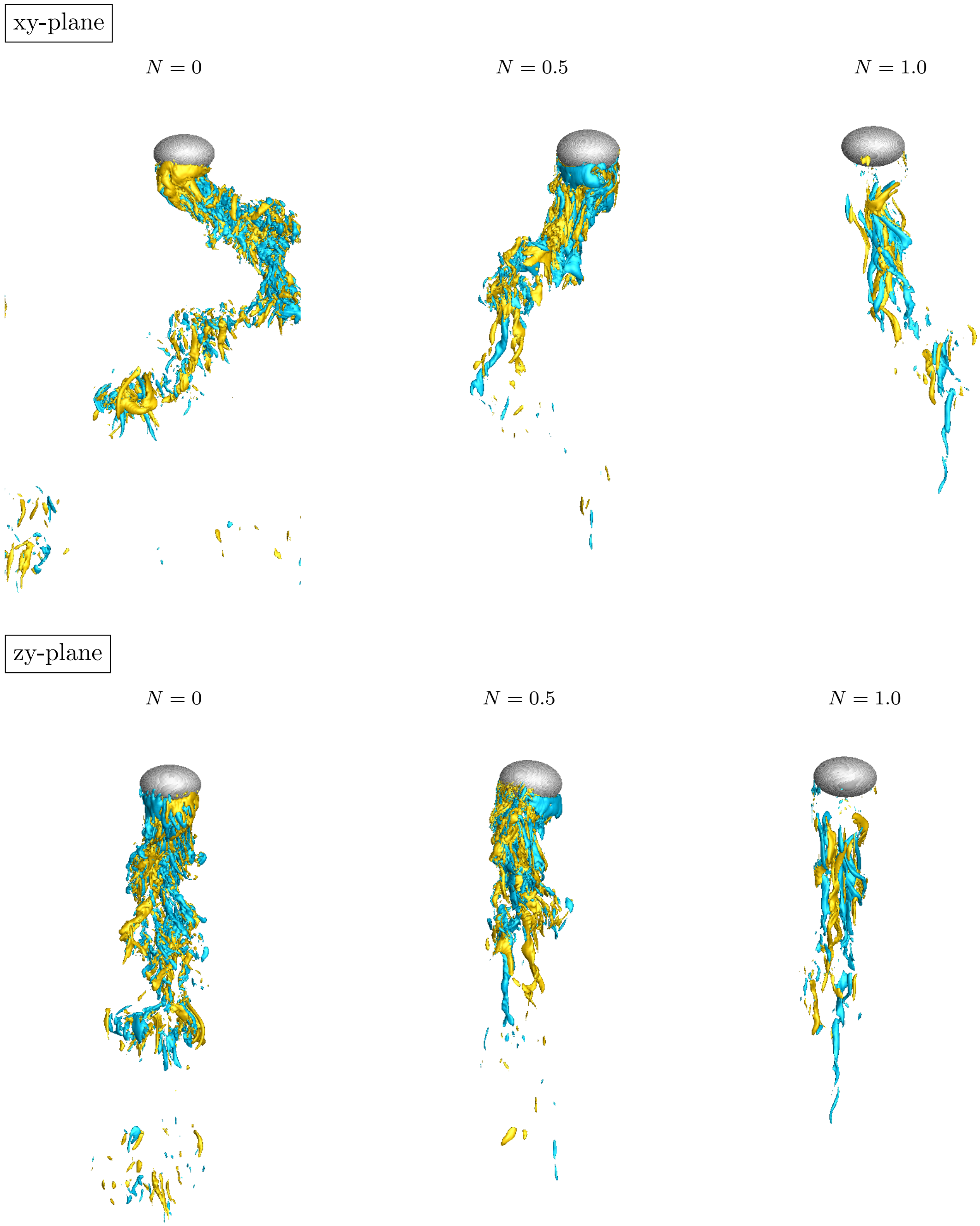

Figure 17: Event C: Iso-contours of $\omega_y d_{eq}/u_{ref} = \pm 6$.

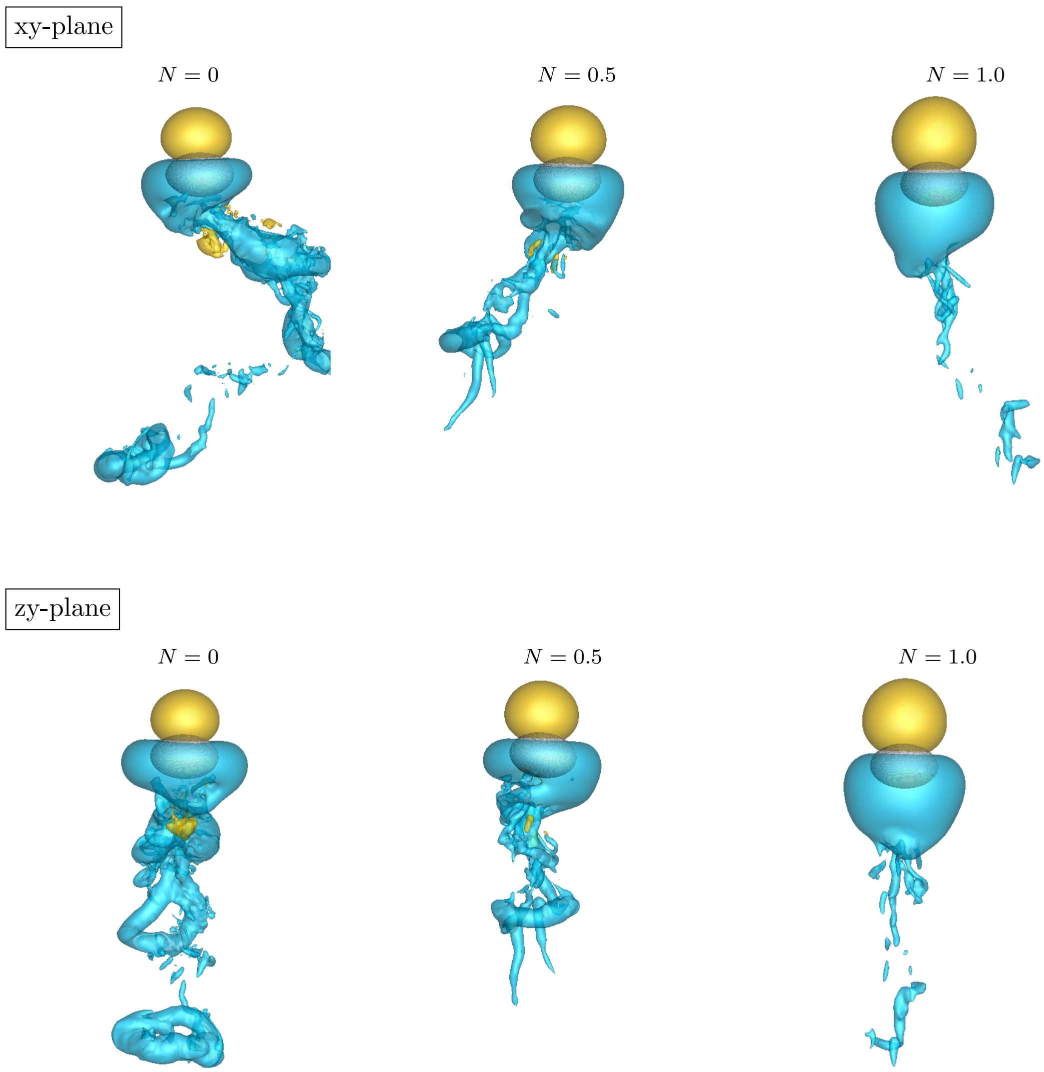

Figure 18: Event C: Iso-contours of pressure with $C_p = p \,/\, \left(\rho_f u_{ref}^2/2\right) = \pm 0.24$.

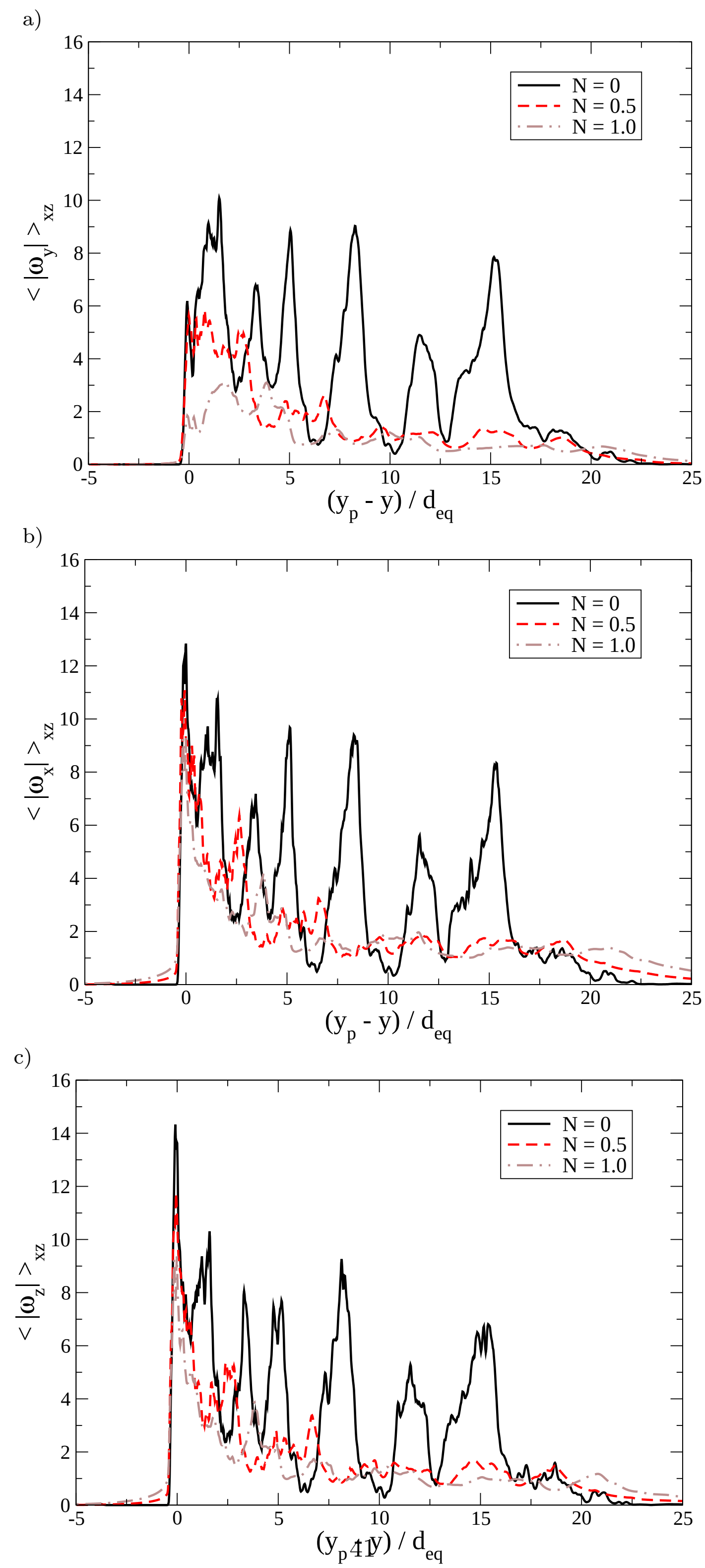

Figure 19: a) Absolute vertical vorticity component $\langle|\omega_y|\rangle_{xz}$ integrated over horizontal planes for the event C indicated in Figures 15, with comparison of the three cases $N = 0,\ 0.5,\ 1.0$. b) Analogous data for the transverse component $\langle|\omega_x|\rangle_{xz}$. c) The same data for the component $\langle|\omega_z|\rangle_{xz}$.

Table 4. Event C: Average magnitude of ω_y compared to total vorticity measured by Γ_y, according to (12), and integral measure of vorticity for all three components.

	$N = 0$	$N = 0.5$	$N = 1.0$
Γ_y	0.471	0.337	0.210
$\sum_{i=1}^{n_y} \langle \lvert\omega_y\rvert \rangle_{xz}^{(i)}$	73.2	36.7	25.8
$\sum_{i=1}^{n_y} \langle \lvert\omega_x\rvert \rangle_{xz}^{(i)}$	75.8	50.4	48.5
$\sum_{i=1}^{n_y} \langle \lvert\omega_z\rvert \rangle_{xz}^{(i)}$	74.5	45.3	39.6

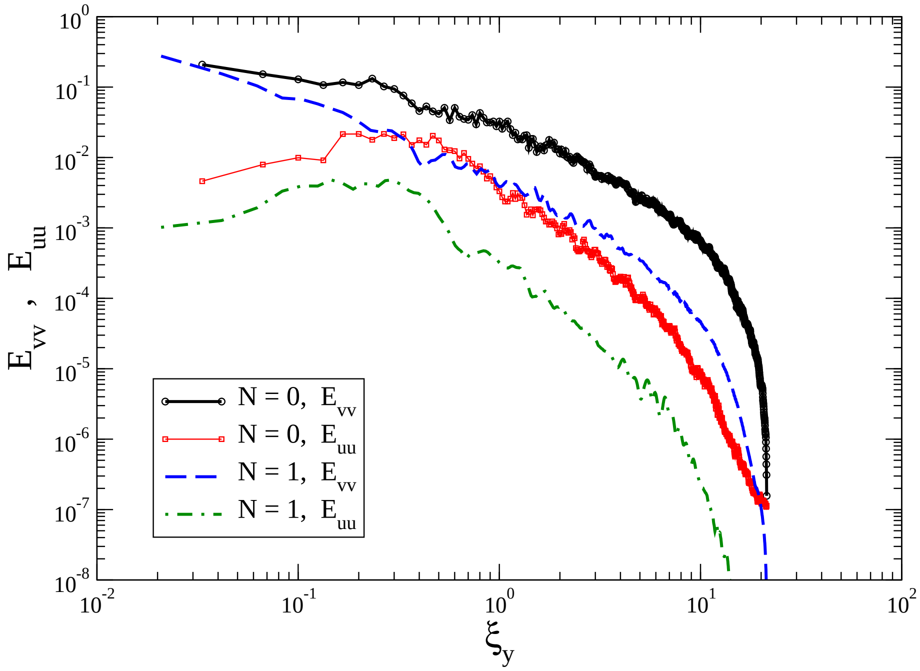

Figure 20: Spatial energy spectra E_{vv} of the vertical velocity component, v, and E_{uu} of the horizontal velocity component, u, along vertical lines with ξ_y the spatial wave number in y. Results for $N = 0$ and $N = 1$.

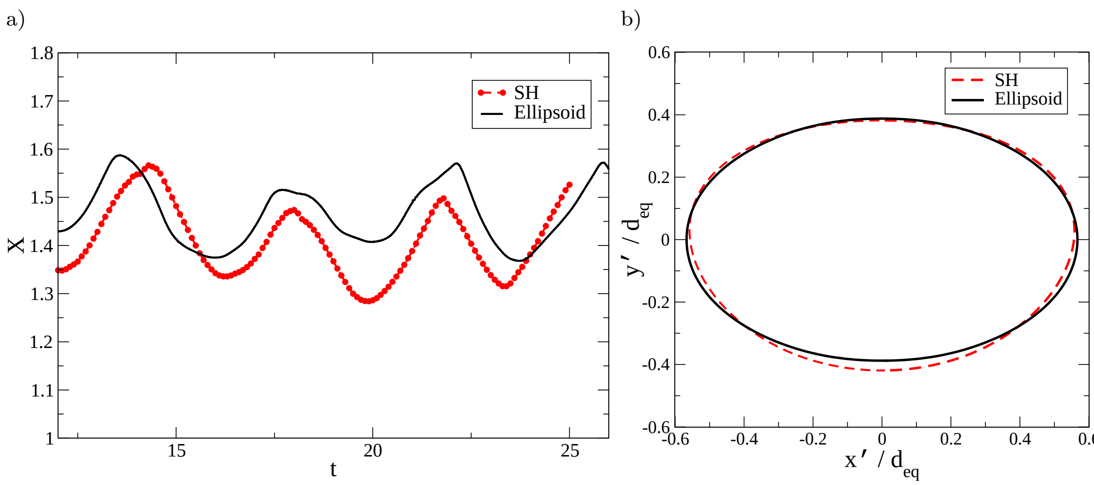

Figure 21: Comparison of results obtained with SH algorithm and with ellipsoidal shape from $X(t) = f(We(t))$, for parameters $G = 2825$, $Eo = 2.5$, $N = 0$: a) Aspect ratio over time. b) Time-averaged bubble shape.

a)

	Ellipsoid	SH	Exp. [22]
Re_t	2871	3037	2879
σ_{Re}	245	307	369
f	0.276	0.281	0.297
$\lvert\phi_z\rvert_{max}$	36°	32°	—
Δ_{xz}/d_{eq}	1.15	1.17	—

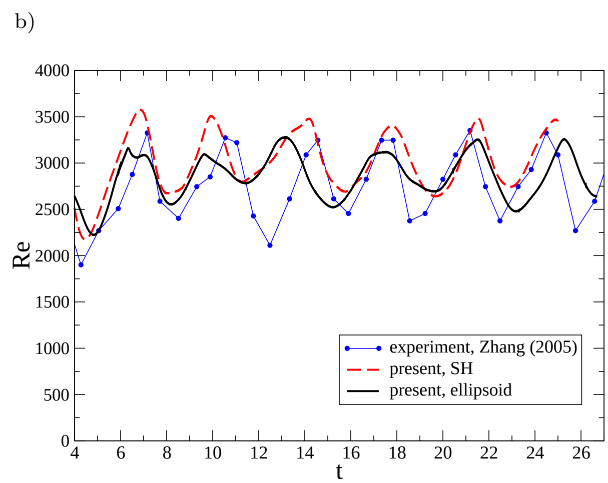

Figure 22: Comparison of spherical harmonics (SH) and ellipsoidal bubble shape for parameters $G = 2825$, $Eo = 2.5$, $N = 0$. a) Bubble dynamics and b) history of bubble rise Reynolds number.

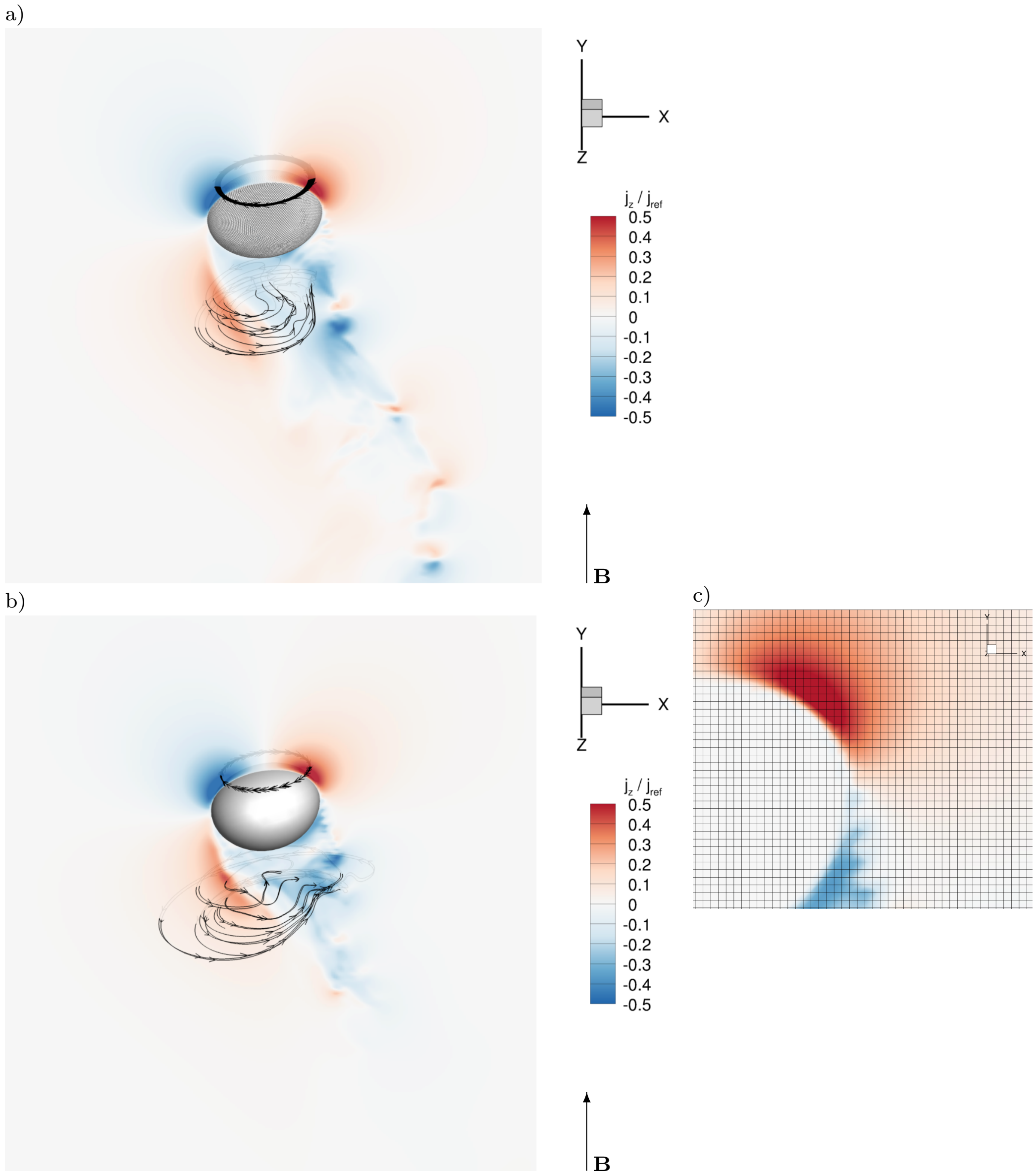

Figure 23: Instantaneous contour of the z-component of the current density, j_z/j_{ref}, with $j_{ref} = \sigma_e u_{ref} B_y$. The values are depicted in an xy-plane through the particle center. The parameters of the simulation are $G = 2825$, $Eo = 2.5$, $N = 1$. a) Ellipsoidal bubble with $\sigma_e = const.$ and selected current streamlines. b) Same plot for an insulating bubble with its shape represented by spherical harmonics at a similar instant in time. c) Detailed view of the phase boundary and mesh for case b).

Table 5. Summary of simulation results for an insulating bubble with its shape represented by spherical harmonics. Numbers in brackets indicate previous simulation results with ellipsoidal bubble shape and constant electric conductivity. $Eo = 2.5$, $G = 2825$

N	Re_t		σ_{Re}		f_{Re}	
0	3037	(2871)	307	(245)	0.281	(0.276)
0.5	—	(2957)	—	(166)	—	(0.233)
1.0	3122	(3132)	125	(90.3)	0.218	(0.181)
2.0	3009		144		0.138	
4.0	2639		148		0.072	

References

[1] A. Prosperetti, Bubbles, Physics of Fluids 16 (6) (2004) 1852–1865.

[2] J. Magnaudet, I. Eames, The motion of high-Reynolds-number bubbles in inhomogeneous flows, Annual Review of Fluid Mechanics 32 (1) (2000) 659–708.

[3] A. de Vries, A. Biesheuvel, L. van Wijngaarden, Notes on the path and wake of a gas bubble rising in pure water, International Journal of Multiphase Flow 28 (11) (2002) 1823 – 1835.

[4] C. Brücker, Structure and dynamics of the wake of bubbles and its relevance for bubble interaction, Physics of Fluids 11 (7) (1999) 1781–1796.

[5] T. Sanada, M. Shirota, M. Watanabe, Bubble wake visualization by using photochromic dye, Chemical Engineering Science 62 (24) (2007) 7264–7273.

[6] P. Saffman, On the rise of small air bubbles in water, Journal of Fluid Mechanics 1 (1956) 249–275.

[7] A. Tomiyama, G. P. Celatab, S. Hosokawaa, S. Yoshida, Terminal velocity of single bubbles in surface tension force dominant regime, International Journal of Multiphase Flow 28 (2002) 1497–1519.

[8] M. Horowitz, C. H. K. Williamson, The effect of Reynolds number on the dynamics and wakes of freely rising and falling spheres, Journal of Fluid Mechanics 651 (2010) 251–294.

[9] K. Ellingsen, F. Risso, On the rise of an ellipsoidal bubble in water: Oscillating paths and liquid-induced velocity, Journal of Fluid Mechanics 440 (2001) 235–268.

[10] G. Mougin, J. Magnaudet, The generalized kirchhoff equations and their application to the interaction between a rigid body and an arbitrary time-dependent viscous flow, International Journal of Multiphase Flow 28 (2002) 1837–1851.

[11] G. Mougin, J. Magnaudet, Wake-induced forces and torques on a zigzagging/spiralling bubble, Journal of Fluid Mechanics 567 (2006) 185–194.

[12] J. Magnaudet, G. Mougin, Wake instability of a fixed spheroidal bubble, Journal of Fluid Mechanics 572 (2007) 311–337.

[13] P. Ern, F. Risso, D. Fabre, J. Magnaudet, Wake-induced oscillatory paths of bodies freely rising or falling in fluids, Annual Review of Fluid Mechanics 44 (1) (2012) 97–121.

[14] K. Timmel, S. Eckert, G. Gerbeth, F. Stefani, Experimental modeling of the continuous casting process of steel using low melting point alloys the LIMMCAST program, ISIJ International 58 (8) (2010) 1134–1141.

[15] K. Timmel, S. Eckert, G. Gerbeth, Experimental investigation of the flow in a continuous casting mould under the influence of a transverse, direct current magnetic field, Metallurgical and Materials Transactions B 42 (2011) 68–80.

[16] C. Zhang, S. Eckert, G. Gerbeth, The flow structure of a bubble-driven liquid metal jet in a horizontal magnetic field, Journal of Fluid Mechanics 557 (2007) 57–82.

[17] J. Stiller, K. Koal, A numerical study of the turbulent flow driven by rotating and travelling magnetic fields in a cylindrical cavity, Journal of Turbulence 10 (2009) 44.

[18] Y. Wang, L. Zhang, Fluid flow-related transport phenomena in steel slab continuous casting strands under electromagnetic brake, Metallurgical and Materials Transactions B 42 (2011) 1319–1351.

[19] R. B. Fdhila, P. Duineveld, The effect of surfactant on the rise of a spherical bubble at high Reynolds and Peclet numbers, Physics of Fluids 8 (2) (1996) 310–321.

[20] E. Loth, Quasi-steady shape and drag of deformable bubbles and drops, International Journal of Multiphase Flow 34 (2008) 523–546.

[21] R. Clift, J. Grace, M. Weber, Bubbles, Drops, and Particles, Dover Publications, 1978.

[22] C. Zhang, S. Eckert, G. Gerbeth, Experimental study of single bubble motion in a liquid metal column exposed to a DC magnetic field, International Journal of Multiphase Flow 106 (2005) 824–842.

[23] Y. Mori, K. Hijikata, I. Kuriyama, Experimental study of bubble motion in mercury with and without a magnetic field, Journal of Heat Transfer 99 (3) (1977) 404–410.

[24] S. Eckert, G. Gerbeth, O. Lielausis, The behaviour of gas bubbles in a turbulent liquid metal magnetohydrodynamic flow. Part I: Dispersion in quasi-two-dimensional magnetohydrodynamic turbulence, International Journal of Multiphase Flow 26 (2000) 45–66.

[25] S. Eckert, G. Gerbeth, O. Lielausis, The behaviour of gas bubbles in a turbulent liquid metal magnetohydrodynamic flow. Part II: Magnetic field influence on the slip ratio, International Journal of Multiphase Flow 26 (2000) 67–82.

[26] Y. Shibasaki, K. Ueno, T. Tagawa, Computation of a rising bubble in an enclosure filled with liquid metal under vertical magnetic fields, ISIJ International 50 (2010) 363–370.

[27] D. Gaudlitz, N. Adams, The influence of magnetic fields on the rise of gas bubbles in electrically conductive liquids, Direct and Large-Eddy Simulation VII, Springer, ERCOFTAC Series 13 (6) (2010) 465–471.

[28] B. Knaepen, R. Moreau, Magnetohydrodynamic turbulence at low magnetic Reynolds number, Annual Review of Fluid Mechanics 40 (2008) 25–45.

[29] T. Boeck, D. Krasnov, E. Zienicke, Numerical study of turbulent magnetohydrodynamic channel flow, Journal of Fluid Mechanics 572 (2007) 179–188.

[30] T. Maxworthy, Experimental studies in magneto-fluid dynamics: Pressure distribution measurements around a sphere, Journal of Fluid Mechanics 31 (1968) 801–814.

[31] J. Fröhlich, S. Schwarz, S. Heitkam, C. Santarelli, C. Zhang, T. Vogt, S. Boden, A. Andruszkiewicz, K. Eckert, S. Odenbach, S. Eckert, Influence of magnetic fields on the behavior of bubbles in liquid metals, The European Physical Journal - Special Topics 220 (1) (2013) 167–183.

[32] T. Kempe, J. Fröhlich, An improved immersed boundary method with direct forcing for the simulation of particle laden flows, Journal of Computational Physics 231 (2012) 3663–3684.

[33] S. Heitkam, S. Schwarz, J. Fröhlich, Simulation of the influence of electromagnetic fields on the drainage in wet metal foam, Magnetohydrodynamics 48 (2) (2012) 313–320.

[34] M. Uhlmann, An immersed boundary method with direct forcing for the simulation of particulate flows, Journal of Computational Physics 209 (2005) 448–476.

[35] T. Kempe, S. Schwarz, J. Fröhlich, Modelling of spheroidal particles in viscous flow, Academy Colloquium Immersed Boundary Methods: Current Status and Future Research Directions. Amsterdam, the Netherlands ISBN: 978-90-6984-590-6.

[36] S. Aland, S. Schwarz, J. Fröhlich, A. Voigt, Modeling and numerical approximations for bubbles in liquid metal, The European Physical Journal - Special Topics 220 (1) (2013) 185–194.

[37] H. Goldstein, J. C.P. Poole, J. Safko, Klassische Mechanik, 3. Auflage, WILEY-VCH Verlag, Weinheim, 2006.

[38] S. Schwarz, J. Fröhlich, Representation of deformable bubbles by analytically defined shapes in an immersed boundary method, Proc. ICNAAM, AIP Conf. Series, edited by T.E. Simos, G.Psihoyios, C.Tsitouras and Z. Anastassi 1479 (2012) 104–108.

[39] S. Schwarz, J. Fröhlich, A temporal discretization scheme to compute the motion of light particles in viscous flows by an immersed boundary method, in preparation.

[40] G. Tryggvason, B. Bunner, A. Esmaeeli, D. Juric, N. Al-Rawahi, W. Tauber, J. Han, S. Nas, Y.-J. Jan, A front-tracking method for the computations of multiphase flow, Journal of Computational Physics 169.

[41] T. Kempe, J. Fröhlich, Collision modelling for the interface-resolved simulation of spherical particles in viscous fluids, Journal of Fluid Mechanics 709 (2012) 445–489.

[42] T. Kempe, A numerical method for interface-resolving simulations of particle-laden flows with collisions, Ph.D. thesis, Technische Universität Dresden, Fakultät für Maschinenwesen (2011).

[43] W.-P. Breugem, A second-order accurate immersed boundary method for fully resolved simulations of particle-laden flows, Journal of Computational Physics 231 (13) (2012) 4469 – 4498.

[44] D. Gaudlitz, Numerische Untersuchung des Aufstiegsverhaltens von Gasblasen in Flüssigkeiten, Ph.D. thesis, Technische Universität München, Fakultät für Maschinenwesen (2008).

[45] M. Simcik, M. Ruzicka, J. Drahos, Computing the added mass of dispersed particles, Chemical Engineering Science 63 (2008) 4580–4595.

[46] L. Schouveiler, A. Brydon, T. Leweke, M. Thompson, Interactions of the wakes of two spheres placed side by side, European Journal of Mechanics - B/Fluids 23 (1) (2004) 137 – 145.

[47] L. Zeng, S. Balachandar, P. Fischer, Wall-induced forces on a rigid sphere at finite Reynolds number, Journal of Fluid Mechanics 536 (2005) 1–25.

[48] T. A. Johnson, V. C. Patel, Flow past a sphere up to a Reynolds number of 300, Journal of Fluid Mechanics 378 (1999) 19–70.

[49] K. Lunde, R. Perkins, Shape oscillations of rising bubbles, Applied Scientific Research 58 (1998) 387–408.

[50] J. Lindt, On the periodic nature of the drag on a rising bubble, Chemical Engineering Science 27 (10) (1972) 1775 – 1781.

[51] G. Yonas, Measurements of drag in a conducting fluid with an aligned field and large interaction parameter, Journal of Fluid Mechanics 30 (1967) 813–821.

[52] S. Schwarz, J. Fröhlich, Numerical simulation of MHD flow around fixed and freely ascending spheres and ellipsoids, 8th PAMIR Int. Conf. on Fundamental and Applied MHD, Borgo, Corsica, France I (2011) 223–227.

[53] T. Wondrak, S. Eckert, G. Gerbeth, K. Klotsche, F. Stefani, K. Timmel, A. Peyton, N. Terzija, W. Yin, Combined electromagnetic tomography for determining two-phase flow characteristics in the submerged entry nozzle and in the mold of a continuous casting model, Metallurgical and Materials Transactions B 42 (2011) 1201–1210.

[54] D. Räbiger, S. Eckert, G. Gerbeth, S. Franke, J. Czarske, Flow structures arising from melt stirring by means of modulated rotating magnetic fields, Magnetohydrodynamics 48 (1) (2012) 213–220.

[55] J. Jeong, F. Hussain, On the identification of a vortex, Journal of Fluid Mechanics 285 (1995) 69–94.

[56] A. Majda, A. Bertozzi, Vorticity and incompressible flow, Cambridge Texts in Applied Mathematics, 2002.

[57] J. Fröhlich, Large Eddy Simulation turbulenter Strömungen, Teubner, 2006.

[58] J. Cano-Lozano, P. Bohorquez, C. Martínez-Bazán, Wake instability of a fixed axisymmetric bubble of realistic shape, International Journal of Multiphase Flow 51 (2013) 11–21.

[59] D. Grigoriadis, S. Kassinos, E. Votyakov, Immersed boundary method for the MHD flows of liquid metals, Journal of Computational Physics 228 (3) (2009) 903–920.

[60] S. Schwarz, J. Fröhlich, Simulation of a bubble chain in a container of high aspect ratio exposed to a magnetic field, The European Physical Journal - Special Topics 220 (1) (2013) 195–205.

[61] S. Heitkam, S. Schwarz, C. Santarelli, J. Fröhlich, Influence of an electromagnetic field on the formation of wet metal foam, The European Physical Journal - Special Topics 220 (1) (2013) 207–214.